



HAL
open science

Carbon isotope fractionation between CO₂ and carbon in silicate melts at high temperature

Hyunjoo Lee, Yves Moussallam, Cyril Aubaud, Giada Iacono-Marziano, Keiji Hammond, Denton Ebel

► **To cite this version:**

Hyunjoo Lee, Yves Moussallam, Cyril Aubaud, Giada Iacono-Marziano, Keiji Hammond, et al.. Carbon isotope fractionation between CO₂ and carbon in silicate melts at high temperature. *Geochimica et Cosmochimica Acta*, 2024, 380, pp.208-219. 10.1016/j.gca.2024.07.015 . insu-04649843

HAL Id: insu-04649843

<https://insu.hal.science/insu-04649843v1>

Submitted on 16 Jul 2024

HAL is a multi-disciplinary open access archive for the deposit and dissemination of scientific research documents, whether they are published or not. The documents may come from teaching and research institutions in France or abroad, or from public or private research centers.

L'archive ouverte pluridisciplinaire **HAL**, est destinée au dépôt et à la diffusion de documents scientifiques de niveau recherche, publiés ou non, émanant des établissements d'enseignement et de recherche français ou étrangers, des laboratoires publics ou privés.

Journal Pre-proofs

Carbon isotope fractionation between CO₂ and carbon in silicate melts at high temperature

Hyunjoo Lee, Yves Moussallam, Cyril Aubaud, Giada Iacono–Marziano, Keiji Hammond, Denton Ebel

PII: S0016-7037(24)00352-1
DOI: <https://doi.org/10.1016/j.gca.2024.07.015>
Reference: GCA 13491

To appear in: *Geochimica et Cosmochimica Acta*

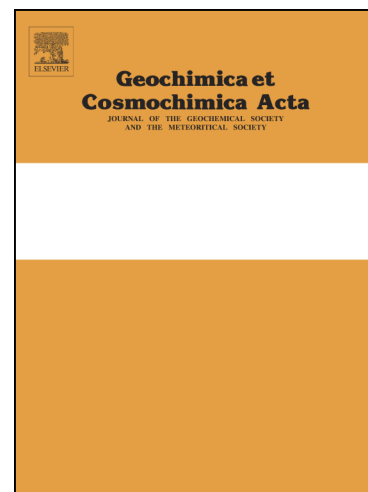
Received Date: 1 March 2024

Accepted Date: 12 July 2024

Please cite this article as: Lee, H., Moussallam, Y., Aubaud, C., Iacono–Marziano, G., Hammond, K., Ebel, D., Carbon isotope fractionation between CO₂ and carbon in silicate melts at high temperature, *Geochimica et Cosmochimica Acta* (2024), doi: <https://doi.org/10.1016/j.gca.2024.07.015>

This is a PDF file of an article that has undergone enhancements after acceptance, such as the addition of a cover page and metadata, and formatting for readability, but it is not yet the definitive version of record. This version will undergo additional copyediting, typesetting and review before it is published in its final form, but we are providing this version to give early visibility of the article. Please note that, during the production process, errors may be discovered which could affect the content, and all legal disclaimers that apply to the journal pertain.

© 2024 Elsevier Ltd. All rights are reserved, including those for text and data mining, AI training, and similar technologies.



Carbon isotope fractionation between CO₂ and carbon in silicate melts at high temperature

Hyunjoo Lee¹, Yves Moussallam^{1,2}, Cyril Aubaud³, Giada Iacono–Marziano⁴, Keiji Hammond², Denton Ebel².

¹ *Lamont–Doherty Earth Observatory, Columbia University, New York, USA*

² *American Museum of Natural History, Department of Earth and Planetary Sciences, NY 10024, New York, USA*

³ *Université Paris Cité, Institut de Physique du Globe de Paris, CNRS, Laboratoire de Géochimie des Isotopes Stables, 1 rue Jussieu, F–75005 Paris, France*

⁴ *ISTO, UMR 7327 Université d’Orléans–CNRS–BRGM, 1a rue de la Ferrollerie, Orléans, France*

Corresponding author: Hyunjoo Lee; hl3507@columbia.edu

Abstract

The isotopic fractionation of carbon between CO₂ gas and silicate melts is a crucial parameter to understand the carbon cycle at the planetary scale that requires accurate quantification. In this study, we conducted experiments to determine the carbon isotope fractionation between CO₂ gas and carbon dissolved in silicate melt at 350 – 420 MPa and 1160 – 1225 °C, across a range of melt compositions. A linear relationship emerges between the fractionation coefficient and the degree of polymerization of the melt (NBO/T; non–bridging oxygens per tetrahedral cation) with the fractionation coefficient increasing for depolymerized melts (e.g., basalt) and decreasing for polymerized melts (e.g., rhyolite):

$$1000\ln\alpha_{\text{gas–melt}}=3.251\times\text{NBO/T}+0.026 \quad (R^2=0.74)$$

or

$$1000\ln\alpha_{\text{gas–melt}}=-0.087\times(\text{SiO}_2+\text{Al}_2\text{O}_3)\text{wt}\%+7.968 \quad (R^2=0.74)$$

These equations enable the calculation of carbon fractionation coefficients in silicate melts, providing a mean to interpret $\delta^{13}\text{C}$ –value measurements in natural volcanic gases and melts through forward and backward modelling of degassing paths from mantle to surface. We hypothesize that the ratio of CO₃²⁻/CO₂ dissolved in the melt is the key parameter behind this relationship. Carbon dissolved as CO₂ molecular transfers to the gas phase with a fractionation coefficient of 0 ‰ whilst carbon dissolved as CO₃²⁻ transfers with a fractionation coefficient of

2.9 ‰. The relationship is calibrated from $NBO/T = 0$ to 0.88, covering most major melt compositions. However, at $NBO/T > 0.88$, as the CO_3^{2-}/CO_2 ratio reaches its maximum in silicate melt, correspondingly the fractionation coefficient reaches its maximum of 2.9 ‰, both are expected to stabilize and remain constant. Carbon isotopic fractionation might hence offer a window into carbon speciation in natural melts.

Keywords: carbon isotopes; carbon isotope fractionation factor; carbon species; $\delta^{13}C$ -value

1. Introduction

Dissolved carbon in magmatic systems is an abundant volatile component that plays a crucial role in determining the initiation depth of partial melting (e.g., Dasgupta and Hirschmann, 2010; Sun and Dasgupta, 2023) and physical properties of mantle melts (e.g., Gaillard et al., 2008; Yoshino et al., 2012). Carbon in the mantle exists in various forms, including diamond (e.g., Jaques et al., 1990), graphite (e.g., Pearson et al., 1994), and carbonate inclusions (e.g., Ionov et al., 1993), as well as fluid inclusions composed of CO_3^{2-} , CH_4 , CO , and COS (e.g., Andersen and Neumann, 2001). Under lithospheric conditions (i.e., 0.5 to 4 GPa, below 1400 °C, and FMQ-1 to +3.5; Solomatova et al., 2020; Katsura, 2022), carbon exists primarily in dissolved forms as either carbonate ion (CO_3^{2-}) or CO_2 molecular in silicate melts (e.g., Blank and Brooker, 1994; Brey and Green, 1976; Mysen et al., 1976). In the coexisting exsolved gas phase, carbon is predominantly found as CO_2 , with lesser amounts of CO (Wardell et al., 2004).

The solubility of CO_2 in silicate melts has a significant positive correlation with depolymerization of the melt and total pressure. To describe the complex relationship between melt composition and CO_2 solubility, researchers have proposed a compositional parameter, Π , (Dixon, 1997; Shishkina et al., 2014) and NBO/T (Non-Bridging Oxygens per Tetrahedral Cations; Brooker et al., 2001), which reflects the ratio between the freely diffusing cations and the tetrahedral network, as a way of measuring the degree of melt polymerization. In addition, experiments have consistently shown that the CO_2 solubility decreases with decreasing pressure across a range of compositions, from felsic to ultramafic and from less than a hundred MPa to several GPa, respectively (e.g., Stolper and Holloway, 1988; Dixon et al., 1995; Jendrzejewski et al., 1997; Newman and Lowenstern, 2002; Shishkina et al., 2014; Moussallam et al., 2015; Eguchi and Dasgupta, 2018). This positive correlation commonly leads to CO_2 saturation in the magma during its journey toward the surface, with very few examples to date of magmatic systems where CO_2 -undersaturated melts have been identified (Javoy and Pineau, 1991; Saal et al., 2002; Michael and Graham, 2015; Le Voyer et al., 2017).

CO_2 has relatively low solubility among the major volatiles (H_2O - CO_2), for example, the maximum solubility of H_2O is 6 wt% and CO_2 is 0.3 wt% for basaltic melt at 400 MPa (Iacono-Marziano et al., 2012), making CO_2 the main driver of degassing and in many cases of magma ascent. Volatile degassing has two end-member processes (e.g., Aubaud, 2022), closed-system degassing and open-system degassing. In closed-system degassing (BED – Batch Equilibrium Degassing, often referred to as equilibrium degassing), the gas phase remains in the system and

isotopic equilibrium is maintained (e.g., Graham et al., 2018). In open–system degassing (FED – Fractional Equilibrium Degassing, often called Rayleigh distillation) exsolved CO₂ escapes from the system instantaneously (e.g., Taylor, 1986).

The carbon stable isotopic ratio in a given phase is expressed with the delta notation defined by Eq. (1) (abbreviation for Equation (1)):

$$\delta^{13}\text{C} = \left(\frac{\left(\frac{^{13}\text{C}}{^{12}\text{C}}\right)_{\text{sample}}}{\left(\frac{^{13}\text{C}}{^{12}\text{C}}\right)_{\text{reference}}} - 1 \right) \times 1000 \quad (1)$$

As CO₂ degasses, carbon isotope fractionation between gas and melt occurs. The fractionation factor ($\alpha_{\text{gas–melt}}$) between gas and melt is defined by Eq. (2). It has been often reported as $\Delta^{13}\text{C}_{\text{eq}}$ using an approximation (Eq. (3)), which is valid only when the absolute values of $\Delta^{13}\text{C}_{\text{eq}}$, $\delta^{13}\text{C}_{\text{gas}}$, and $\delta^{13}\text{C}_{\text{melt}}$ are all less than 10 ‰ (O’Neil, 1986; Sharp, 2017). Hereafter, we will call $1000\ln\alpha_{\text{gas–melt}}$ and the previously reported $\Delta^{13}\text{C}_{\text{eq}}$ as the fractionation coefficient.

$$\alpha_{\text{gas–melt}} = \frac{1000 + \delta^{13}\text{C}_{\text{gas}}}{1000 + \delta^{13}\text{C}_{\text{melt}}} \quad (2)$$

$$1000\ln\alpha_{\text{gas–melt}} \approx \Delta^{13}\text{C}_{\text{eq}} = \delta^{13}\text{C}_{\text{gas}} - \delta^{13}\text{C}_{\text{melt}} \quad (3)$$

Degassed CO₂ shows a higher $\delta^{13}\text{C}$ –value compared to the melt. Several studies on carbonate, including experimental work (Chacko et al., 1991; Scheele and Hoefs, 1992; Rosenbaum, 1994; Appora, 1998; Petschnig et al., 2024) and theoretical calculations (Bottinga, 1969; Chacko et al., 1991; Deines, 2004), have shown that the fractionation coefficient decreases by 4 ‰ to 2 ‰ with increasing temperatures within the range of 700–1200 °C. The fractionation coefficient has been reported from experimental studies to be close to 0 ‰ for rhyolitic melt (Blank, 1993), and anywhere from +1.8 to 4.7 ‰ in basaltic melts (Javoy et al., 1978; Matthey, 1991; Matthey et al., 1990; Trull et al., 1992). The variation in the fractionation coefficient in the compositional range between rhyolite and basalt remains unexplored.

While carbon isotope fractionation between gas and melt can be used to reconstruct the magma degassing path, the lack of constraints on the fractionation coefficient has led to inconsistency between studies. The higher $\delta^{13}\text{C}$ –value of degassed CO₂ results in a subsequent decrease in the $\delta^{13}\text{C}$ –value of the residual melt. As both BED and FED progress, the depletion of $\delta^{13}\text{C}$ –value of CO₂ within the residual melt and coexisting gas will display a distinct evolutionary path with a steeper depletion of $\delta^{13}\text{C}$ –value in FED compared to BED. For example, Pineau and Javoy (1983) proposed a two–step degassing model to explain the $\delta^{13}\text{C}$ –value depletion of carbon dissolved in MORB, with gradual $\delta^{13}\text{C}$ –value depletion at higher C and steep depletion at lower C. This model has been applied to the $\delta^{13}\text{C}$ –value variations in MORB (e.g., Cartigny et al., 2001) as well as arc environments (e.g., Shaw et al., 2004). However, due to the lack of agreement in the fractionation coefficient of mafic melts, $\delta^{13}\text{C}$ –value of volcanic gas and basaltic rocks were modeled to generate degassing paths using either extremes or varying fractionation coefficient. For example, Matthey et al. (1989) used average +2 ‰ (range +1 to +4.4 ‰), Paonita et al. (2012) chose +3 ‰, while several recent studies employed +3.5 ‰ (e.g., Cartigny et al., 2001; Pineau et al., 2004; Aubaud, 2022).

Carbon isotope fractionation in submarine volcanic glasses has been used to reconstruct pre-eruptive carbon concentration in the melt, but this estimate is highly dependent on the fractionation coefficient. The procedure measures CO₂ concentration in the gas or melt and assumes a $\delta^{13}\text{C}$ -value of the initial melt (e.g., -4.5 ‰; Cartigny et al., 2001). Pre-eruptive carbon can then be calculated by modeling its degassing path (detailed calculations are provided by Cartigny et al., 2008). Estimates of Cartigny et al. (2008) (600 – 55000 ppm CO₂) and Aubaud et al. (2004) (2700 ppm CO₂) align with pre-degassed carbon estimates obtained through CO₂/Nb ratio and “popping rock”, respectively. Macpherson et al. (2005) found that the Kolbeinsey Ridge melt, the northern part of the Mid-Atlantic Ridge, has a pre-eruptive CO₂ concentration (~400 ppm) lower than primitive MORB, suggesting potential degassing before equilibration at 2.7 – 3.0 km below the seafloor, and indicating a two-stage degassing process. All these calculations rely heavily on knowledge of the fractionation coefficient. Macpherson et al. (2005) tested two fractionation coefficient values of +2.3 ‰ and +4.5 ‰ in their calculations, finding the +2.3 ‰ value to be the only one consistent with their observed relationships between CO₂ and noble gases.

Previous experimental studies on mafic melts yielded inconsistent CO₂ solubility and mass balance and sometimes failed to provide critical information such as melt composition or its final water content. In the first attempt to decipher fractionation coefficient, Javoy et al. (1978) reported a range of 4.0 – 4.6 ‰ for oceanic tholeiite. However, their dissolved CO₂ in the glass at saturation was inconsistent, ranging from 0.73 wt% to 2.56 wt% under identical conditions (750 MPa, 1280 °C). At these conditions, a CO₂ solubility of 2.56 wt% is unexpectedly high, which might imply a formation of reduced carbon formation potentially influencing carbon isotope fractionation. Two experiments using different brands of oxalic acid as a carbon source produced inconsistent CO₂ yields, 0.5 and 2.6 wt%. Finally, their step-heating measurement showed a significant contribution of low-temperature carbon released below 600 °C, which could have been from reduced carbon form (i.e., graphite) or surface carbon contamination (Mattey et al., 1989). Mattey et al. (1990) conducted experiments on sodamelilite (NaCaAlSi₂O₇) and reported a smaller fractionation coefficient of 2.2 – 2.7 ‰. They recovered only 20 – 92 % of the expected gaseous CO₂, but showed that this CO₂ loss has a negligible effect on the isotope fractionation coefficient. In a subsequent study, Mattey (1991) conducted an experiment on MORB melt composition obtaining results consistent with their prior research (fractionation coefficient = 1.8 – 2.2 ‰), but suffered CO₂ loss during the experiment as well. Trull et al. (1992) reported fractionation of 1.9 – 4.7 ‰ (average 3.5 ± 1.0 ‰) in experiments on MORB composition but provided limited information on their initial melt composition. The most recent experimental study, Appora (1998), investigated carbon isotope fractionation between CO₂ and carbonate melts, finding a fractionation coefficient of 3.5 ‰, which is probably not directly applicable to silicate melt.

One major challenge in interpreting previous experimental studies is the absence of available H₂O measurements on the resulting glasses, except for Blank (1993). The presence of H₂O in the melt plays a critical role in silicate structure and CO₂ behavior (e.g., Moussallam et al., 2016a; Solomatova et al., 2020; Stolper and Holloway, 1988). In one hydrous experiment conducted by Javoy et al. (1978), precise input material quantities were not provided, hindering accurate H₂O content estimation. Even though all of the experiments on mafic melt experiments (except the one above) are nominally H₂O-free, trace amounts of H₂O (a few hundred ppm to a weight percent) can still be present due to ubiquitous atmospheric water and hydrogen diffusion in experiments. Mattey (1991) and Mattey et al. (1990) have detected H₂O peaks in their infrared spectra,

emphasizing the importance of measuring H₂O content in the glass, even in nominally H₂O-free experiments.

In light of these challenges, this study examines the effect of composition on the carbon isotope fractionation coefficient between gas and melt and fills the compositional gap between rhyolite and basalt. To achieve this goal, we conducted a series of experiments ranging from andesite to basanite composition at 350 – 420 MPa and 1160 – 1225 °C to examine the effect of melt structure on the gas–melt isotopic fractionation coefficient.

2. Methods

2.1. Experimental Methods

The starting materials used in this study included: natural basanite from El Hierro mixed with variable amounts of SiO₂ and Al₂O₃ to produce compositions ranging from basanite to andesite (NBO series), natural basalt from Mt.Etna (Etna series), and synthetic compositions made of a four-oxide (SiO₂, Al₂O₃, MgO, and CaO) mixtures (Simple series). To ensure homogeneity and remove any initial volatiles present, all starting materials were first fused at 1300 °C in a Pt crucible at 0.1 MPa in air for 2 hours, then quenched. The retrieved glass was crushed and re-melted once more under the same conditions for an additional 2 hours. The fused glasses were examined using Fourier transform infrared spectroscopy (FTIR) to confirm that they were volatile-free (see 2.2.3).

Experiments were conducted in two internally heated pressure vessels, one at the Institut des Sciences de la Terre d'Orléans (ISTO) and the other at the American Museum of Natural History (AMNH) (Table 1). The variations in vessel size led to differences in capsule size and material quantity, with ISTO's larger vessel allowing for the use of more materials (350 mg for ISTO and 150 mg for AMNH) and larger capsules. Gold–palladium (Au₈₀–Pd₂₀) tubes (5 mm o.d. / 4.5 mm i.d. / 35 mm long for ISTO and 4.0 mm o.d. / 3.5 mm i.d. / 20 mm long for AMNH) were used in all experiments. Cut and annealed capsules were initially welded flat at one end for the ISTO experiment and triple-crimped then welded for AMNH. Then, the capsules were ultrasonically cleaned in dichloromethane for 10 minutes to remove any organic carbon that might have been present on the capsule's surface (Mattey et al., 1989) and then stored at 110 °C prior to use. The capsules were prepared by filling them with starting material, deionized water (1 – 4 wt%), and dihydrated oxalic acid (C₂H₂O₄·2H₂O) (1–6 wt% of CO₂). The δ¹³C-value of the dihydrated oxalic acid used is -20.58 ‰ for the Etna series, -26.68 ‰ for the NBO and Simple series, and was determined by repeated measurements with an elemental analyzer coupled isotope ratio mass spectrometer (see 2.2.2) with a standard deviation of ± 0.14 ‰. The final welding process utilized flat welding with tungsten electrodes to minimize the introduction of additional carbon into the capsule.

The detailed experimental conditions are listed in Table 1. Pure argon was used as a pressure medium (leading to oxygen fugacities above FMQ+1, where FMQ is the fayalite–magnetite–quartz buffer; Webster and De Vivo, 2002 for AMNH; Gaillard et al., 2003 for ISTO). This high oxidation state ensured that all carbon exists in oxidized forms, the CO₂ molecular or CO₃²⁻ (Wardell et al., 2004). Most of the experiments were conducted at superliquidus conditions, except

for samples CI_IPGP_NBO_3_6 and CI_IPGP_NBO_5_2 (see 3.1). After reaching the target P–T, the experiments were equilibrated for 18 – 24 hours. Experiments were then quenched isobarically by drop–quench at a rate of approximately 100 °C/s (Di Carlo et al., 2006).

Table 1

Conditions of IHPV experiments and resulting phase assemblages

Sample	Pressure (MPa)	Temperature (°C)	Duration (h)	Run at	Phase assemblages
CI_AMNH_NBO_1_3	347	1202	18	AMNH	Silicate melt + gas
CI_AMNH_NBO_2	348	1168	20	AMNH	Silicate melt + gas
CI_AMNH_NBO_2_2	350	1201	22	AMNH	Silicate melt + gas
CI_AMNH_NBO_3	351	1189	48	AMNH	Silicate melt + gas
CI_AMNH_NBO_3_1	351	1182	24	AMNH	Silicate melt + gas
CI_AMNH_NBO_3_2	351	1160	23	AMNH	Silicate melt + gas
CI_AMNH_NBO_3_4	350	1200	24	AMNH	Silicate melt + gas
CI_AMNH_NBO_4	349	1187	24	AMNH	Silicate melt + gas
CI_AMNH_NBO_5	349	1200	24	AMNH	Silicate melt + gas
CI_IPGP_NBO_1_2	400	1225	24	ISTO	Silicate melt + gas
CI_IPGP_NBO_3_6	393	1225	22	ISTO	Silicate melt + Fe-oxide + gas

CI_IPGP_NBO_5_2	393	1225	22	ISTO	Silicate melt + Fe-oxide + gas
CI_NBO_2_2	400	1225	24	ISTO	Silicate melt + gas
CI_NBO_3_3	400	1225	24	ISTO	Silicate melt + gas
ETNA-3-2	419	1200	24	ISTO	Silicate melt + gas
ETNA-3-2bis	419	1200	24	ISTO	Silicate melt + gas
ETNA-3-3	419	1200	24	ISTO	Silicate melt + gas
ETNA-4-1	371	1200	24	ISTO	Silicate melt + gas

2.2. Analytical Methods

The gas phase was extracted from the sealed capsule and analyzed first, followed by the isotopic analysis of the dissolved CO₂ in the glass using an elemental analyzer coupled to an isotope ratio mass spectrometer. The concentration of volatiles (CO₂-H₂O) and the major element composition of the glass were analyzed using FTIR and electron microprobe, respectively. The occurrence of crystals within experimental samples was checked by scanning electron microscopy (SEM).

2.2.1. $\delta^{13}\text{C}$ -value analysis in the gas phase

The amount of CO₂ in the gas and its isotopic signature ($\delta^{13}\text{C}_g$) were analyzed at the Institut de Physique du Globe de Paris (IPGP), France. Post experiment, each sealed capsule was pierced under vacuum in a dedicated extraction line. After piercing, the gas released from the capsule was passed over CuO enclosed in a Pt foil to catalyze the oxidation reaction at 450 °C. This process was carried out to ensure the conversion of any CO and H₂ present to CO₂ and H₂O (although the amount of CO and H₂ was negligible). The extracted gas was then captured in a cold trap at -196 °C. After 15 minutes of trapping, any remaining gas (mostly N₂) was pumped off. CO₂ was then released by setting the temperature of the cold trap at -135 °C to retain only H₂O. CO₂ was cold trapped again and then released in a calibrated volume with a Baratron capacitance manometer to measure its total amount in the range 0–10 μmol . For larger amounts (>10 μmol), CO₂ was

measured with a mercury manometer ($\pm 5\%$). The gas is finally trapped in a Pyrex® glass tube for isotopic analysis, which was performed using a dual inlet Delta Plus XP isotope ratio mass spectrometer (IRMS) equipped with a microvolume ($\pm 0.03\%$).

2.2.2. $\delta^{13}\text{C}$ -value analysis in the glass

The isotopic signature of CO_2 dissolved in the glass ($\delta^{13}\text{C}_m$) was determined using a Costech elemental analyzer (EA) coupled with a ConFlo IV and Thermo Scientific Delta V plus isotope ratio mass spectrometer (IRMS) at Lamont–Doherty Earth Observatory. Thin glass shards were carefully hand-picked under a microscope to avoid entrapped gas bubbles. Glass shards were then weighed on a microbalance ($\pm 0.001\text{ mg}$), placed into a $3.2 \times 4\text{ mm}$ tin capsule, and kept in a desiccator until analysis.

The enclosed samples were dropped into a $980\text{ }^\circ\text{C}$ oven and then combusted at $\sim 1700\text{ }^\circ\text{C}$ with excess oxygen (25 ml/min) over a chromium (III) oxide catalyst. Helium was used as the carrier gas (100 ml/min). Silvered cobaltous/cobaltic oxide inside the quartz combustion tube ensured the complete conversion of sample carbon to CO_2 and the removal of residual halogens or sulfur. After the separation of the CO_2 peaks through a gas chromatography (GC) column ($55\text{ }^\circ\text{C}$), each sample was analyzed by IRMS.

The $\delta^{13}\text{C}_m$ -values for each sample were calibrated by three-point regression using standards USGS24 ($\delta^{13}\text{C} = -16.04\text{ }^\circ\text{‰}$, VPDB), USGS40 ($\delta^{13}\text{C} = -26.77\text{ }^\circ\text{‰}$, VPDB), and USGS41 ($\delta^{13}\text{C} = 37.63\text{ }^\circ\text{‰}$, VPDB) with an average precision of $0.16\text{ }^\circ\text{‰}$. All measurements of carbon isotope standards agree with the accepted values reported by the United States Geological Survey (USGS). To test for instrument performance and linear drift, one standard set was analyzed for every 10 samples. The measurement error of the $\delta^{13}\text{C}$ -value, calculated to be $\pm 0.14\text{ }^\circ\text{‰}$, was determined based on repeated measurements of the carbon source, oxalic acid.

The instrument was calibrated using acetanilide ($\text{C}_8\text{H}_9\text{NO}$) to determine the bulk carbon content ($\pm 0.2\text{ }^\circ\text{‰}$, $R^2 = 0.9999$). Additional calibration was performed with a mixture of oxalic acid and SiO_2 containing 70, 20, 5, 2, 1, 0.75, 0.5, and 0.25 wt% of CO_2 ($R^2 = 0.9999$) to properly account for the characteristics of the glass material to be analyzed. A set of standards was inserted for each daily run. Linear regression was used to derive the calibrated total carbon content based on the true concentration of the mixture series. Based on the reproducibility of the mixture series, the error in CO_2 estimation was calculated to be $\pm 7.3\text{ }^\circ\text{‰}$.

2.2.3. Glass analysis by Fourier transform infrared spectroscopy (FTIR)

H_2O and CO_2 concentrations in the retrieved glasses were measured using a Thermo Nicolet iN10 Fourier transform infrared (FTIR) spectrometer at Lamont–Doherty Earth Observatory. The instrument was purged with dry and CO_2 -scrubbed air. The measurements were made on a liquid nitrogen-cooled MCT–A detector.

Glass chips were doubly polished with alumina-coated polishing paper. Their thickness ranged from 20 to 100 μm . The glass chips were washed with acetone to remove any crystal bond before they were placed on a CaF_2 plate for measurement. Thickness was measured using the reflectance method ($\pm 3 \mu\text{m}$; Nichols and Wysoczanski, 2007).

Absorption spectra were collected from each sample in the 400 – 8000 cm^{-1} range with 256 scans and 1 cm^{-1} resolution in transmitted mode. The aperture size was 100 μm in width and height. To confirm the homogeneity of H_2O and CO_2 contents in the glass, a minimum of 3 spots were analyzed for each sample.

Total H_2O content was calculated using the intensity of the OH^- stretching band at around 3550 cm^{-1} . The CO_2 doublet peaks around 1515 cm^{-1} and 1435 cm^{-1} were used to determine the CO_2 concentration. Baseline correction is performed by subtracting the spectra of chemically matched devolatilized glasses (i.e., our starting compositions fused in air). The absorption coefficient of CO_2 was determined using the $\text{Na}/(\text{Na}+\text{Ca})$ molar ratio of the glass composition (Dixon and Pan, 1995). The absorption coefficient of H_2O was determined to be 63 $\text{L}/\text{mol}/\text{cm}$ (Dixon et al., 1995). To calculate the glass density, both H_2O and CO_2 were taken into account (Bourgue and Richet, 2001; Lesher and Spera, 2015).

2.2.4. Electron Microprobe

Electron microprobe analyses were conducted at AMNH using a Cameca SX5–Tactis to determine the major element composition of the experimental glasses, utilizing a 15 kV accelerating voltage, a defocused beam of 10 μm , 4 nA beam current for Na (10 s count time) and 10 nA for other elements (20 s count time). Na was analyzed first in order to have a minimum of Na loss during the analysis. The instrument was calibrated using natural and synthetic mineral standards and glasses including: potassium feldspar (Al, Si, and K), rutile (Ti), fayalite (Fe), rhodonite (Mn), olivine (Mg), anorthite (Ca), jadeite (Na), and apatite (P). Ten random spots were analyzed to obtain an average value for each glass and the errors are reported as the standard deviation of the 10 repeated analyses. The samples were imaged with Scattered Electron Microscope (SEM) with Bruker Quantax Quad at AMNH.

3. Results

3.1. Phase assemblage and texture

Glass recovered from capsules was in the form of thin shards of brown–black to green–black color. The color was generally uniform. The exsolved vapor inclusions completely trapped in the glass were rarely observed under the microscope. Quench crystals were not observed under the 500 magnifications of the microscope and SEM images (Fig. S1). IPGP_NBO_3_6 and CI_IPGP_NBO_5_2 included opaque Fe–oxides (less than 1 % in volume) that grew during the experiment (Fig. S1).

3.2. Major element and volatile composition of glasses

Glass compositions analyzed by electron microprobe are shown in Table 2. Fe is reported as Fe²⁺O total and Fe³⁺/FeT ratio is calculated by equation from [Kress and Carmichael \(1991\)](#) assuming FMQ+1 for all experiments. CO₂ dissolved in the glass (CO_{2glass}), H₂O dissolved in the glass (H₂O_{glass}), δ¹³C–value of the gas (δ¹³C_g) and glass (δ¹³C_m) are shown in Table 3. CO_{2glass} in Table 3 is measured by FTIR, except for type “Simple” (CI_NBO_2_2 and CI_NBO_3_3), in which it was obtained by EA, due to the absence of known absorption coefficient for FTIR on this Si–Al–Ca–Mg composition. CO_{2glass} measured by EA (Table S2) is in good agreement with CO_{2glass} measured by FTIR (Fig. 1). CO_{2glass} varies from 500 to 3600 ppm, increasing with the degree of depolymerization (Fig. 2). H₂O dissolved in the glass measured by FTIR varies from 1 to 3 wt%.

3.3. Carbon isotope composition of gases and melts

δ¹³C–value of the gas and melt diverge from the carbon source as the depolymerization degree increases from 0.36 to 0.88 (Fig. 3), resulting in an increase in the fractionation coefficient (ranges 0.53 – 4.69). The fractionation coefficient is calculated from the δ¹³C–value of the melt and of the coexisting gas as 1000lnα_{g–m} (see introduction for the definition). The fractionation coefficient shows a linear relationship with composition (Fig. 4). The linear correlation derived is below:

$$1000\ln\alpha_{g-m}=3.251\times\text{NBO}/T+0.026 \quad (R^2=0.74) \quad (4)$$

$$1000\ln\alpha_{g-m}=-0.087\times(\text{SiO}_2+\text{Al}_2\text{O}_3)\text{wt}\%+7.968 \quad (R^2=0.74) \quad (5)$$

where NBO/T is calculated on a hydrous basis:

$$\text{NBO}/T = 2 \times \frac{X_{\text{H}_2\text{O}}+X_{\text{K}_2\text{O}}+X_{\text{Na}_2\text{O}}+X_{\text{CaO}}+X_{\text{MgO}}+X_{\text{FeO}}+X_{\text{MnO}}-X_{\text{Al}_2\text{O}_3}-X_{\text{Fe}_2\text{O}_3}}{X_{\text{SiO}_2}+2\times X_{\text{Al}_2\text{O}_3}+X_{\text{TiO}_2}+2\times X_{\text{Fe}_2\text{O}_3}} \quad (6)$$

The highest 1000lnα_{g–m} value observed in sample ETNA3–3 appears to deviate from the trend line. The δ¹³C_{glass}–value in this sample (–24.23 ± 0.14 ‰; this study) was independently measured by secondary ion mass spectrometry (SIMS) ([Lee et al., 2024](#); –23.0 ± 1.3 ‰). The δ¹³C_{glass}–value from SIMS gives a less deviating fractionation coefficient of 3.4 ± 1.3 ‰, although both δ¹³C_{glass}–values are within the error range.

Table 2

Compositions of the glass (in wt%) analyzed by electron microprobe after the experiment is normalized to 100 minus the H₂O and CO₂ concentrations measured by FTIR. The

unnormalized raw analytical sum of the averaged measurements is shown in Table S1. The values are an average of 10 repeated analyses. Standard deviations are reported in parentheses.

Sample	Type	SiO ₂	TiO ₂	Al ₂ O ₃	FeO ^a	Mn O	Mg O	CaO	Na ₂ O	K ₂ O	P ₂ O ₅	Total	Fe ³⁺ /FeT ^b
CI_AMNH_NBO_1_3	NBO	57.7 7 (0.5 7)	2.73 (0.0 4)	18.7 9 (0.3 6)	6.86 (0.1 9)	0.10 (0.0 4)	3.48 (0.0 5)	6.12 (0.1 1)	2.47 (0.0 7)	1.06 (0.0 2)	0.63 (0.0 5)	97.4 1	0.19
CI_AMNH_NBO_2	NBO	56.1 8 (0.2 3)	3.12 (0.0 3)	16.9 6 (0.1 0)	8.03 (0.2 0)	0.12 (0.0 6)	3.85 (0.0 5)	6.85 (0.0 6)	2.93 (0.0 7)	1.29 (0.0 2)	0.67 (0.0 7)	96.9 8	0.20
CI_AMNH_NBO_2_2	NBO	55.0 0 (0.2 6)	3.17 (0.0 5)	17.9 6 (0.0 8)	7.82 (0.1 7)	0.12 (0.0 5)	3.94 (0.0 7)	7.07 (0.0 7)	2.95 (0.0 9)	1.27 (0.0 2)	0.70 (0.0 3)	96.8 8	0.20
CI_AMNH_NBO_3	NBO	52.0 6 (0.1 9)	3.61 (0.0 4)	17.1 8 (0.0 7)	8.76 (0.1 7)	0.15 (0.0 7)	4.55 (0.0 6)	8.12 (0.0 6)	3.31 (0.0 6)	1.44 (0.0 2)	0.82 (0.0 3)	96.9 9	0.2 1
CI_AMNH_NBO_3_1	NBO	51.1 7 (0.3 4)	3.58 (0.0 4)	17.6 9 (0.1 0)	9.25 (0.1 3)	0.19 (0.0 8)	4.50 (0.0 5)	8.10 (0.0 5)	3.31 (0.0 9)	1.40 (0.0 4)	0.81 (0.0 9)	97.1 9	0.2 1
CI_AMNH_NBO_3_2	NBO	51.2 8 (0.2 2)	3.60 (0.0 6)	17.5 1 (0.1 0)	9.39 (0.2 3)	0.17 (0.0 5)	4.47 (0.0 7)	8.05 (0.0 8)	3.34 (0.1 2)	1.41 (0.0 2)	0.78 (0.0 4)	97.0 9	0.2 1
CI_AMNH_NBO_3_4	NBO	51.1 7	3.56 (0.0 3)	17.9 1	9.11 (0.1 9)	0.11 (0.0 5)	4.50 (0.0 5)	8.10 (0.0 7)	3.31 (0.1 0)	1.41 (0.0 2)	0.81 (0.0 5)	96.9 3	0.2 1

		(0.1 6)	(0.1 1)										
CI_AMNH_NBO_4	NBO	49.0 3 (0.2 6)	3.98 (0.0 4)	16.1 8 (0.0 5)	10.5 4 (0.1 3)	0.19 (0.0 6)	4.98 (0.0 6)	8.90 (0.0 9)	3.70 (0.1 2)	1.64 (0.0 2)	0.87 (0.0 7)	97.4 8	0.2 2
CI_AMNH_NBO_5	NBO	45.8 7 (0.2 5)	4.51 (0.0 3)	15.5 1 (0.1 0)	11.3 7 (0.2 0)	0.20 (0.0 5)	5.58 (0.0 7)	10.1 9 (0.0 4)	3.98 (0.2 3)	1.80 (0.0 3)	0.99 (0.0 6)	97.4 5	0.2 3
CI_IPGP_NBO_1_2	NBO	57.9 4 (0.4 0)	2.67 (0.0 5)	18.7 3 (0.1 9)	7.06 (0.2 0)	0.12 (0.0 7)	3.30 (0.0 8)	5.95 (0.0 9)	2.53 (0.0 8)	1.11 (0.0 2)	0.59 (0.0 4)	97.8 1	0.1 9
CI_IPGP_NBO_3_6	NBO	54.1 4 (0.2 4)	2.62 (0.1 1)	17.5 6 (0.2 8)	6.89 (0.1 4)	0.14 (0.0 3)	4.31 (0.0 4)	8.42 (0.1 7)	3.65 (0.1 5)	1.48 (0.0 3)	0.78 (0.0 7)	97.9 4	0.2 2
CI_IPGP_NBO_5_2	NBO	48.6 7 (0.2 5)	3.60 (0.0 4)	16.2 9 (0.0 5)	7.28 (0.2 7)	0.20 (0.0 6)	5.55 (0.0 4)	10.7 6 (0.0 7)	4.58 (0.1 0)	1.94 (0.0 3)	1.12 (0.0 6)	98.1 1	0.2 5
CI_NBO_2_2	Simpl e	65.3 3 (0.3 6)	0.03 (0.0 1)	16.7 5 (0.0 6)	0.09 (0.0 6)	0.03 (0.0 4)	6.62 (0.0 9)	11.0 9 (0.0 7)	0.03 (0.0 1)	0.02 (0.0 1)	0.01 (0.0 1)	98.5 9	0.2 1
CI_NBO_3_3	Simpl e	60.3 7 (0.2 8)	0.02 (0.0 2)	15.4 5 (0.1 1)	0.06 (0.0 5)	0.03 (0.0 4)	8.97 (0.0 7)	14.9 9 (0.0 9)	0.07 (0.0 2)	0.02 (0.0 0)	0.02 (0.0 2)	98.3 9	0.2 3

ETNA-3-2	Etna	48.8 0 (0.2 5)	1.68 (0.0 8)	16.6 6 (0.1 5)	9.85 (0.0 7)	0.19 (0.0 3)	6.43 (0.0 8)	10.6 6 (0.1 2)	3.29 (0.1 9)	1.91 (0.0 3)	0.54 (0.0 4)	97.0 1	0.2 3
ETNA-3-2bis	Etna	48.6 8 (0.1 7)	1.66 (0.0 5)	16.2 7 (0.1 4)	10.6 3 (0.0 8)	0.18 (0.0 3)	6.35 (0.0 5)	10.5 3 (0.0 9)	3.30 (0.1 4)	1.87 (0.0 7)	0.53 (0.0 6)	96.8 5	0.2 2
ETNA-3-3	Etna	49.2 2 (0.6 1)	1.66 (0.0 5)	16.3 2 (0.1 6)	9.87 (0.2 8)	0.17 (0.0 5)	6.37 (0.0 6)	10.6 4 (0.0 9)	3.29 (0.1 2)	1.89 (0.0 4)	0.56 (0.0 7)	97.9 2	0.2 3
ETNA-4-1	Etna	51.1 7 (0.4 4)	1.70 (0.0 5)	17.1 7 (0.1 6)	5.97 (0.2 0)	0.18 (0.0 4)	6.67 (0.0 5)	11.1 5 (0.1 2)	3.45 (0.2 4)	1.97 (0.0 5)	0.57 (0.0 4)	96.9 2	0.2 4

^a Fe is reported as Fe²⁺O total.

^b Fe³⁺/FeT ratio is calculated using the equation by [Kress and Carmichael \(1991\)](#) assuming FMQ+1.

Table 3

Final CO₂ and H₂O concentrations in the glass, δ¹³C-value in the glass and gas phases, and resulting isotopic fractionation coefficient. 1-sigma error is shown.

Sample	CO ₂ _{glass}	H ₂ O _{glass}	δ ¹³ C _{glass}	δ ¹³ C _{gas}	1000lnα _{g-m}
	(ppm) ±	(wt% ±)	(‰) ±	(‰) ±	±

CI_AMNH_NBO_1_3_755	149	2.52	0.44	-27.35	0.17	-26.23	0.03	1.15	0.18	
CI_AMNH_NBO_2_1003	113	2.92	0.35	-27.49	0.16	-26.01	0.03	1.52	0.17	
CI_AMNH_NBO_2_2_1144	148	3.01	0.13	-27.32	0.15	-26.30	0.03	1.05	0.15	
CI_AMNH_NBO_3_1167	132	2.89	0.19	-27.49	0.07	-26.07	0.03	1.46	0.08	
CI_AMNH_NBO_3_1_1397	80	2.68	0.22	-27.68	0.19	-25.98	0.02	1.74	0.20	
CI_AMNH_NBO_3_2_1501	177	2.76	0.05	-27.70	0.19	-26.02	0.02	1.73	0.19	
CI_AMNH_NBO_3_4_1357	167	2.94	0.09	-27.89	0.06	-26.17	0.02	1.77	0.06	
CI_AMNH_NBO_4_1874	344	2.33	0.14	-27.01	0.15	-25.68	0.03	1.37	0.16	
CI_AMNH_NBO_5_3147	301	2.23	0.15	-27.48	0.01	-25.57	0.02	1.97	0.02	
CI_IPGP_NBO_1_2_772	71	2.12	0.32	-27.03	0.37	-26.52	0.02	0.53	0.38	
CI_IPGP_NBO_3_6_827	139	1.98	0.11	-28.12	0.29	-26.43	0.02	1.74	0.30	
CI_IPGP_NBO_5_2_2320	245	1.66	0.15	-28.39	0.05	-25.54	0.03	2.93	0.06	
CI_NBO_2_2_561	559	1.36	0.03	-27.61	0.61	-26.52	0.01	1.12	0.62	
CI_NBO_3_3_520	322	1.56	0.03	-28.09	0.37	-26.43	0.03	1.71	0.38	
ETNA-3-2	3343	101	2.66	0.06	-22.70	0.15	-20.25	0.02	2.50	0.15

ETNA-3-2bis	3335	54	2.81	0.02	-22.19	0.15	-19.58	0.02	2.67	0.15
ETNA-3-3	3580	208	1.73	0.07	-24.23	0.15	-19.65	0.03	4.69	0.16
ETNA-4-1	2396	66	2.84	0.08	-22.31	0.15	-18.88	0.03	3.50	0.16

4. Discussion

4.1. Data reliability

A critical consideration is whether the experiments reached equilibrium. First, we stress that the experimental systems remained entirely closed with no evidence of open system behavior or leakage. The recovered capsules did not show any weight loss after the experiment (Table S2). Extracted gas was mostly CO₂ (17 – 276 μmole) with minor traces of H₂O (background level), as expected (Table S2). The recovered glasses exhibited consistent homogeneity, with a relative standard deviation below 5 % in 10 repeated analyses, regardless of their location within the sample (Table 2). Previous experiments under P–T–X conditions similar to ours demonstrated that they reached equilibrium by “reversal test”, i.e. first equilibrating at high pressure and then re-equilibrating at lower pressure for 20 minutes to 2.5 hours (Mattey, 1991; Dixon et al., 1995). Reversal experiments showed CO₂ solubility, δ¹³C–value of the glass and gas results consistent with forward experiments, indicating that a duration of 20 minutes at 1400 °C is sufficient to reach equilibrium. We are, therefore, confident that the duration of our experiment (18 – 48 hours) allowed us to reach elemental and isotopic equilibrium for carbon.

Some of the primary challenges in analyzing the δ¹³C–value in experimental glasses are the presence of sub–solidus carbonate precipitates, CO₂ gas exsolution in the bubbles during quench, or carbon adsorption (Mattey, 1991; Macpherson et al., 1999). Several results support the successful recovery of δ¹³C–value in the glass. No solid carbonate phases were observed under the microscope and with the SEM. Isobaric drop quenching was used to ensure rapid quenching and minimize post–experiment CO₂ exsolution from the melt to the gas bubble (e.g., Paillat et al., 1992). Few large bubbles were observed in the recovered glasses, due to volatile saturation, but they were easily avoidable by selecting thin shards under the microscope. Although the presence of submicroscopic gas bubbles cannot be excluded, the strong correspondence between dissolved CO₂ contents measured by FTIR and EA (Fig. 1), strongly suggests that the contributions of the solid carbonate, gas bubbles, and surface carbon are minor compared to the predominant dissolved CO₂ in the glass.

The question of whether a reduced form of carbon existed in the gas or melt is significant due to its potential to substantially impact solubility, fractionation properties, and carbon interactions with the melt structure. Pure argon was used as the pressure medium for the experiment, which is estimated to induce an oxygen fugacity above FMQ+1 in the IHPV (Webster and De Vivo, 2002; Gaillard et al., 2003). This environment allows carbon to dissolve in the silicate melt in its oxidized

form (CO_3^{2-} or CO_2 molecular) (e.g., Wardell et al., 2004). We didn't observe any reduced carbon species (e.g., CH_4 , CO) in the FTIR spectra, and the good agreement between $\text{CO}_{2\text{glass}}$ measured by FTIR and EA (Fig.1) suggests the absence of reduced carbon species in the glass. Moreover, our CO_2 solubilities are comparable with those predicted by CO_2 solubility models at the given P–T–X (Iacono–Marziano et al., 2012) (Fig. S2), corroborating the absence of reduced carbon as well as other major carbon species besides CO_3^{2-} in the glass.

4.2. Compositional effect

Our experiments, conducted at 1160 – 1225 °C and 350 – 420 MPa, investigate the $\delta^{13}\text{C}$ –value fractionation coefficient between gas and silicate melt ($1000\ln\alpha_{\text{g-m}}$) over a range of compositions from andesitic basalt to basanite. Fig. 4 illustrates the relationships between melt composition and $1000\ln\alpha_{\text{g-m}}$ derived from both our study and the literature (Mattey et al., 1990; Mattey, 1991; Blank, 1993). In reviewing previous experiments, we have excluded the measurement from Javoy et al. (1978) and Trull et al. (1992) because of the absence of melt composition and $\text{H}_2\text{O}_{\text{glass}}$ information, which significantly affects silicate melt structures. In addition, the analyses of Javoy et al. (1978) included low–temperature carbon from the step–heating method for $\delta^{13}\text{C}_{\text{glass}}$, possibly originating from surface carbon or contamination (e.g., Mattey et al., 1989). In CO_2 –sodamelilite experiments (Mattey et al., 1990), we excluded the results that showed carbonate precipitation during the experiment to focus solely on the fractionation between CO_2 and silicate melt. Given these considerations, we have excluded these measurements from further examination.

Due to the complexity of the various carbon species in the silicate melt and the species–specific fractionation behavior, the gas–melt fractionation factor can be expressed as the sum of the mole fractions by species multiplied by each fractionation factor (Deines, 2004). In the gas, oxidized experimental conditions allowed CH_4 and CO to be excluded and only CO_2 to be included (e.g., Gaillard et al., 2003; Wardell et al., 2004; Webster and De Vivo, 2002). CO_2 is dissolved in the silicate melt as either carbonate ion (CO_3^{2-}) or CO_2 molecular (Brey and Green, 1976; Mysen et al., 1976; Blank and Brooker, 1994), $\text{CO}_3^{2-}/\text{CO}_2$ ratios decreasing with the polymerization of the melt (detailed in discussion later in this section). Carbon isotopic fractionation in silicate melt is therefore a combination of two fractionations between gas and melt: (1) CO_2 gas– CO_2 molecular in the melt and (2) CO_2 gas– CO_3^{2-} in the melt.

It should be noted that equilibrium between volatile gases and silicate melt is achieved by diffusion processes. Reaction of the CO_2 molecular– CO_2 gas is expected to dominate over CO_3^{2-} – CO_2 gas in the diffusion process (e.g., Spickenbom et al., 2010). The diffusion coefficient of bulk CO_2 in silicate melts is nearly invariant over a wide range of compositions (e.g., Sierralta et al., 2002). This is because the increase in CO_2 molecular diffusivity from rhyolite to basalt melts is countered by a concurrent decrease in the fraction of CO_2 dissolved as CO_2 molecular with respect to that dissolved as CO_3^{2-} (Nowak et al., 2004). The diffusion coefficient of CO_2 is one order of magnitude (tholeiite) to four orders of magnitude (rhyolite) higher than that of CO_3^{2-} (Nowak et al., 2004; Spickenbom et al., 2010). The activation energy of CO_3^{2-} for diffusion is also more than twice as high (80.6 kJ/mol for CO_3^{2-} and 34.5 kJ/mol for CO_2 molecular), regardless of the composition range (Guillot and Sator, 2011).

In addition, CO_3^{2-} is much more strongly bonded to the silicate structure than CO_2 molecular, in other words, it has a lower mobility in the melt and between the melt and gas phase. Both CO_2 molecular and CO_3^{2-} interact with non-bridging oxygen (NBO, bound to one network former or to a network modifier cation) and bridging oxygen (BO, bound to two network formers) in the silicate structure (Guillot and Sator, 2011; Moussallam et al., 2016b). However, the distance from the carbon to the nearest oxygen is more than twice as short for CO_3^{2-} (1.25Å) than for the CO_2 molecular (2.65Å) according to molecular dynamics simulation for carbon in silicate melts (Guillot and Sator, 2011).

While CO_3^{2-} exhibits limited mobility due to its lower diffusivity and stronger bonding, a rapid interconversion between the CO_2 molecular and CO_3^{2-} has been observed, surpassing the rate of CO_2 transport in the melt. This is demonstrated by the experiment showing a constant $\text{CO}_3^{2-}/\text{CO}_2$ ratio throughout diffusion profiles measured by FTIR (Sierralta et al., 2002). Molecular dynamics simulations further support this observation, indicating that every diffusing CO_2 molecular into the melt undergoes numerous interconversions before exiting from the melt (Guillot and Sator, 2011). The homogenous equilibrium of the CO_2 gas- CO_3^{2-} reaction is maintained during the diffusion process in the silicate melt. Consequently, the carbon exchange between the melt and the gas is controlled by the CO_2 molecular, involving the conversion of CO_3^{2-} to CO_2 molecular in the melt rather than direct diffusion of CO_3^{2-} out of the melt.

The $\delta^{13}\text{C}$ -value fractionation between CO_2 gas and CO_2 molecular in the melt appears to be negligible, as shown by the experiment with a rhyolitic composition that contains only CO_2 molecular in the melt (Fig. 3). Given the similar geometry of CO_2 gas and CO_2 molecular, minimal fractionation is expected. The close correspondence in antisymmetric stretching frequencies observed in IR and NMR studies between the CO_2 molecular in glass (2350cm^{-1} , 125 ppm) and CO_2 gas (2348cm^{-1} , 124.2 ppm) further supports the similar geometry of the molecular structure between the two (e.g., Kohn et al., 1991). In addition, the comparable activation energy between the molecular CO_2 and Ar suggests that molecular CO_2 behaves as an inert molecule which has no isotopic fractionation between gas and melt at equilibrium (e.g., Marty and Humbert, 1997).

In contrast, during CO_3^{2-} - CO_2 molecular conversion in the melt, ^{13}C is enriched in the CO_2 molecular rather than in CO_3^{2-} . This is explained by isotope fractionation rules (Grootes et al., 1969), which is the preference of the heavy isotope ^{13}C for lower coordination numbers and symmetric molecules, CO_2 . Considering the lower mobility of CO_3^{2-} and the rapid conversion between the two species in the melt (see reasoning above), we expect the isotope fractionation to occur primarily between the CO_3^{2-} and CO_2 molecular in the melt, rather than between CO_3^{2-} and CO_2 gas. Consequently, the bulk fractionation may be indicative of $\text{CO}_3^{2-}/\text{CO}_2$ species ratio in the melt.

Infrared spectroscopy studies of quenched silicate glasses have shown that CO_2 exists exclusively as the CO_2 molecular in rhyolite (Fogel and Rutherford, 1990) and as CO_3^{2-} in basalt (Fine and Stolper, 1986; Shishkina et al., 2014). In intermediate compositions, infrared spectroscopy studies showed that dissolved CO_2 in the glass exists as a combination of both with a systematic decrease in $\text{CO}_3^{2-}/\text{CO}_2$ ratio towards the felsic composition (Brey, 1976; Fogel and Rutherford, 1990; King and Holloway, 2002; Duncan and Dasgupta, 2014, 2015; Muth et al., 2020). However, the speciation in quenched glasses is not an accurate representation of that of silicate melts. Experimental studies (Morizet et al., 2001; Nowak et al., 2003), molecular dynamic

studies (Guillot and Sator, 2011; Moussallam et al., 2016b), and a synchrotron in situ infrared study (Konschak and Keppler, 2014) all show that, whilst it may not be preserved in the glass, even depolymerized melts such as basalts contain non-negligible amounts of molecular CO_2 at high temperature.

We argue that carbon isotope fractionation between the gas and melt phases is markedly less affected by quenching than the $\text{CO}_3^{2-}/\text{CO}_2$ ratio. This is based on the understanding that CO_2 exchange between the gas and melt phases occurs primarily by diffusion at magmatic temperatures (see reasoning above). It should be noted that the speciation conversion “within” the melt does not reflect the ongoing isotopic exchange “between” the gas and melt phases during quenching. Considering the time scale of quenching (~ 10 seconds), a diffusion during quenching should be minimal, as the diffusion length scale during quenching is at most a few microns according to the diffusion coefficient in basaltic melts (Zhang et al., 2007). Therefore, the isotope signatures in the quenched glass is likely to reflect the high temperature equilibrium state prior to cooling.

Eq. (4) and (5) are calibrated from $\text{NBO}/\text{T} = 0$ to 0.88, covering most major melt compositions at the earth’s surface and we interpret these relationships as the result of dissolved carbon speciation going from entirely CO_2 molecular in rhyolite ($\text{NBO}/\text{T} \approx 0$) to predominantly CO_3^{2-} in alkalic basalt and basanite ($\text{NBO}/\text{T} \approx 0.88$). At $\text{NBO}/\text{T} > 0.88$, however, we expect the relationship to stabilize and remain constant as the majority of the carbon will be dissolved as CO_3^{2-} by then and the $\text{CO}_3^{2-}/\text{CO}_2$ ratio won’t increase significantly with further depolymerisation. This interpretation is consistent with the experimental results of Petschnig et al., (2024) on nephelinite– CO_2 fractionation at 1175 °C and 0.3 GPa (Fig. 5).

H_2O induces depolymerization of the silicate melt, increasing NBO/T (e.g., Stolper, 1982). An increase in fractionation coefficient is simply expected with H_2O addition, however, the paucity of data on the effect of the H_2O content on the carbon speciation hinders a conclusive understanding of its effect on carbon isotope fractionation. Furthermore, the limited range of H_2O content (1.4 – 3.0 wt%) in this study makes it difficult to accurately estimate its effect on carbon isotope fractionation.

4.3. Temperature effect

Experimental results and literature data are plotted against $10^6/\text{T}^2$ in Fig. 6. Theoretical calculation studies between pure carbonate and gas CO_2 predict a decrease in fractionation coefficient with increasing temperature, as expected for an equilibrium process (Chacko et al., 1991; Deines, 2004; Petschnig et al., 2024). This trend is also expected from the changes in species ratios in the melt. A decrease in temperature and an increase in pressure is expected to result in an increase in the $\text{CO}_3^{2-}/\text{CO}_2$ ratio (Fine and Stolper, 1985; Guillot and Sator, 2011; Konschak and Keppler, 2014; Morizet et al., 2015), which should lead to an expected increase in fractionation coefficient.

However, over the temperature range of our study (1160–1225 °C) and previous experiments (1200–1400 °C; Matthey et al., 1990; Matthey, 1991), no trend in fractionation coefficient with

temperature at constant composition is discernible, showing a discrepancy from the pure carbonate–CO₂ gas system. This discrepancy may be due to different fractionation mechanisms between pure carbonate and silicate melt systems. This is also shown by the disagreement with the predicted line of pure carbonate system and an experiment between nephelinite melt and CO₂ gas by [Petschnig et al. \(2024\)](#).

4.4. Application

The equation derived from this study allows the calculation of fractionation coefficients. Here, comparisons are made with fractionation coefficients derived from natural samples. [Graham et al. \(2018\)](#) estimated the fractionation coefficient in MORB from the East Pacific Rise (EPR). Assuming closed–system degassing, a linear regression slope between $\delta^{13}\text{C}$ –value and CO₂ fraction of vesicle yields a fractionation coefficient of 3.3 ‰ (± 0.5 ‰). Using Eq. (4) and (5), an average fractionation coefficient of 2.4 ‰ and 2.3 ‰ (range 2.3 – 2.5 ‰ and 2.2 – 2.3 ‰, respectively) was calculated based on their 74 basalt composition from [Goss et al. \(2010\)](#) (Table S3). The higher fractionation coefficient estimated by [Graham et al. \(2018\)](#) (3.3 ‰) indicates that the assumption of closed system degassing may not be valid and that open system degassing could be potentially involved, leading to greater carbon isotope depletion. In the extensively degassed central Lau Basin, most $\delta^{13}\text{C}$ –values and CO₂ concentrations in the glass data were consistent with a fractional equilibrium degassing (FED) line plotted with a fractionation coefficient of 2.3 ‰ ([Macpherson and Matthey, 1994](#)), which is comparable to our calculation of 2.3 ‰ from Eq. (4) (H₂O and melt composition from [Kent et al., 2002](#) and [Pearce et al., 1994](#); Table S3).

[Macpherson et al. \(2005\)](#) used a fractionation coefficient of 2.3 ‰ to reconstruct pre–eruptive CO₂ concentration at the Kolbeinsey Ridge. This fractionation coefficient (2.3 ‰) reproduces the observed relationships between CO₂ and noble gases, and is in a very good agreement with the values of 2.5 ‰ and 2.4 ‰ that we calculate from Eq. (4) and (5), respectively (Table S3 for the composition used for the calculation). [Barry et al. \(2014\)](#) used a fractionation coefficient of 4.2 ‰ to estimate 531 ppm pre–eruptive CO₂ in the melt of Iceland with an inferred initial $\delta^{13}\text{C}$ –value of –2.5 ‰. This initial $\delta^{13}\text{C}$ –value is relatively high compared to the typical mantle $\delta^{13}\text{C}$ –values (–4 to –5 ‰; e.g., [Javoy and Pineau, 1991](#); [Cartigny et al., 1998](#)). We calculate from Eq. (4) a fractionation coefficient of 2.6 ‰, which would yield 1542 ppm CO₂ in the pre–eruptive melt with an initial $\delta^{13}\text{C}$ of –4.1 ‰ (Table S3 and Fig. S3). This threefold higher CO₂ estimate suggests the presence of a carbon–rich source beneath Iceland, such as recycled material (e.g., [Brandon et al., 2007](#); [Halldórsson et al., 2016](#); [Miller et al., 2019](#)), in addition to the CO₂–poor depleted MORB mantle (DMM).

As the carbon isotope fractionation coefficient varies with melt composition, it should be expected to change as magma evolves during fractional crystallization. To investigate the effect of magma evolution on $\delta^{13}\text{C}$ –value changes during degassing, we performed fractional crystallization simulation using MELTS (Fig. 7 and Table S4). The initial setting was Etna melt inclusion composition ([Kamenetsky et al., 2007](#)), 600 MPa, and 1180 °C. The SiO₂ content ranges from 44 wt% to 52 wt%, resulting in a decrease in fractionation coefficient from 2.9 ‰ to 1.1 ‰. Both the BED and FED show a steeper decrease in $\delta^{13}\text{C}$ –value during the early stages of crystallization, with smaller isotope fractionation as magma evolves. A higher $\delta^{13}\text{C}$ –value difference between

gas–melt in depolymerized melt further suggests that observing a higher $\delta^{13}\text{C}$ –value in volcanic gas may not necessarily indicate an increased source $\delta^{13}\text{C}$ –value but could reflect mafic recharge of the magma chamber.

The $\delta^{13}\text{C}$ –value of carbon dissolved in the melt ($\delta^{13}\text{C}_m$) provides valuable insights into identifying the carbon source and determining the initial carbon isotope ratio and carbon concentration by tracing degassing pathways. $\delta^{13}\text{C}_m$ is influenced by a combination of 1) BED, 2) FED, 3) kinetic fractionation, 4) carbonate precipitation from the melt, 5) mixing with organic sediment, and 6) assimilation with surrounding carbonate (Fig. 8).

$$\delta^{13}\text{C}_m = M \times \{ \delta^{13}\text{C}_i + \Delta^{13}\text{C}_{\text{eq}}(F-1) + \Delta^{13}\text{C}_{\text{eq}} \ln(F) + \Delta^{13}\text{C}_{\text{kin}} \ln(F) + \Delta^{13}\text{C}_{\text{carb}}(F-1) \} + S \times \delta^{13}\text{C}_{\text{org}} + L \times \delta^{13}\text{C}_{\text{lime}} \quad (7)$$

$\delta^{13}\text{C}_i$, the initial $\delta^{13}\text{C}$ –value, may differ from the source; most mantle values are estimated in a range of -4 ‰ to -5 ‰ (e.g., Javoy and Pineau, 1991; Cartigny et al., 1998). $\Delta^{13}\text{C}_{\text{eq}}$ (fractionation coefficient) can be derived from Eq. (4) in this study, taking into account the melt composition of each system. F is the remaining CO_2 fraction in the silicate melt relative to the initial. BED and Rayleigh distillation induce a decrease in $\delta^{13}\text{C}$ –values with different slopes. Conversely, kinetic fractionation is a diffusive mass–dependent reaction, resulting in the gas having a smaller $\delta^{13}\text{C}$ –value than the melt, and consequently increasing $\delta^{13}\text{C}_m$. Since kinetic fractionation is a mass–dependent reaction, $\Delta^{13}\text{C}_{\text{kin}}$ varies with the diffusing carbon species: -11.1 ‰ for CO_2 molecular and -8.7 ‰ for CO_3^{2-} . Carbonate precipitation from the melt has minimal effect on $\delta^{13}\text{C}$ –values due to the near–zero fractionation ($\Delta^{13}\text{C}_{\text{carb}}=0.39$ ‰; Petschnig et al., 2024) between silicate melt and precipitated carbonatite. Organic sediment significantly reduces $\delta^{13}\text{C}$ –values, whereas marine limestone typically has values close to 0 ‰ ($\delta^{13}\text{C}_{\text{org}}=-30$ ‰ and $\delta^{13}\text{C}_{\text{lime}}=0$ ‰; Sano and Marty, 1995). M , S , and L are the mole fractions of silicate melts, organic sediment and limestone (or carbonate), respectively with $M+S+L=1$ (Sano and Marty, 1995). Understanding these processes enables accurate interpretation of $\delta^{13}\text{C}$ –value for carbon dynamics.

5. Conclusions

We conducted experiments at 350 – 420 MPa and 1160 – 1225 °C across a range of compositions from basanite to andesite to derived carbon isotope fractionation coefficient between CO_2 gas and carbon dissolved in the silicate melt.

We found a positive linear correlation between the carbon fractionation coefficient and the composition or the degree of depolymerization of the melt.

$$1000 \ln \alpha_{\text{gas-melt}} = 3.251 \times \text{NBO}/T + 0.026 \quad (R^2=0.74)$$

and

$$1000 \ln \alpha_{\text{g-m}} = -0.087 \times (\text{SiO}_2 + \text{Al}_2\text{O}_3) \text{wt}\% + 7.968 \quad (R^2=0.74)$$

These equations allow the calculation of the carbon isotope fractionation coefficient for the most commonly occurring silicate melts ranging from basanite to rhyolite. At $NBO/T > 0.88$ we expect the isotope fractionation coefficient to remain constant at $\sim 2.9\text{‰}$ as we hypothesize that the ratio of CO_3^{2-}/CO_2 dissolved in the melt is the key parameter behind this relationship. Carbon isotopic fractionation might hence offer a window into carbon speciation in natural melts.

Melt temperature and H_2O could be of secondary importance to determine the carbon isotope fractionation coefficient compared to melt composition, but their effects should be investigated further.

Acknowledgments

This study is funded by FORED (Foundation for Overseas Resources Development) scholarship program. We would like to thank Celine Martin for her assistance with the microprobe analysis. Special thanks are extended to Wei Huang for her valuable contributions to the elemental analyzer analysis. We are very grateful to Rajdeep Dasgupta and Colin Macpherson for their insightful comments and reviews, which greatly improved the manuscript.

Data Availability

Data are available through the supplementary materials as well as Mendeley Data at DOI: 10.17632/vp6ngrjzdy.4

CRedit authorship contribution statement

Hyunjoo Lee: Conceptualization, Data curation, Investigation, Methodology, Supervision, Validation, Visualization, Writing – original draft, Writing – review & editing. **Yves Moussallam:** Conceptualization, Formal Analysis, Funding acquisition, Methodology, Project administration, Resources, Supervision, Validation, Writing – review & editing. **Cyril Aubaud:** Conceptualization, Formal Analysis, Methodology, Resources, Validation, Writing – review & editing. **Giada Iacono–Marziano:** Conceptualization, Formal Analysis, Methodology, Resources, Validation, Writing – review & editing. **Keiji Hammond:** Methodology, Resources, Validation. **Denton Ebel:** Resources, Supervision, Writing – review & editing, Validation.

Appendix A. Supplementary Material

The supplementary material includes Figure S1, which presents SEM images of the experimental glasses, Figure S2, providing a comparison between CO_2 dissolved in the glass and the expected solubility using a model. Table S1 is unnormalized analytical total of major composition data, and Table S2 details the mass difference before and after each experiment,

$\text{CO}_{2\text{glass}}$ measurements by elemental analyzer, and the extracted amounts of CO_2 and H_2O gas. Table S3 is the composition data used to calculate the fractionation coefficient in section 4.4, and Table S4 is the MELTs data used in Fig. 7. Table S5 integrates this study and the previous experimental data on carbon isotope fractionation between gas and silicate melt.

Figure captions

Fig. 1. CO_2 dissolved in the glass ($\text{CO}_{2\text{glass}}$) measured by EA versus FTIR in ppm. The dashed line is the 1 to 1 line. Only “Etna” and “NBO” are shown on the plot, as the FTIR result of “Simple” is missing due to the lack of a known absorption coefficient for this composition. Shades represent the average 1–sigma deviation between two measurements. CO_2 dissolved in the glass measured by FTIR and bulk CO_2 measured by EA follow a general 1 to 1 correlation, which confirms that the EA measurements were not contaminated by additional surface carbon, CO_2 in gas bubbles, or other suspicious reduced materials.

Fig. 2. $\text{CO}_{2\text{glass}}$ in ppm as a function of NBO/T (non–bridging oxygens to tetrahedral cations), which shows a general increase in $\text{CO}_{2\text{glass}}$ with the depolymerization degree. $\text{CO}_{2\text{glass}}$ is measured by FTIR except “Simple” series (see result) and associated error is a standard deviation of repeated measurement.

Fig. 3. This plot shows the $\delta^{13}\text{C}$ –value of gas and glass in each experiment relative to the initial $\delta^{13}\text{C}$ –value of the carbon source (dashed line). Only “NBO” and “Simple” are shown on the plot, since oxalic acid with a different $\delta^{13}\text{C}$ –value was used for “Etna” ($\delta^{13}\text{C}=-20.58\text{‰}$).

Fig. 4. The dashed line represents a linear regression of data from our study and the literature (Mattey et al., 1990; Mattey, 1991; Blank, 1993). The legend is shown in the top left corner. A) NBO/T plotted against $1000\ln\alpha_{g-m}$ which represents the $\delta^{13}\text{C}$ –value fractionation between gas and melt. The linear regression equation shown in the bottom right corner is Eq. (4) and R^2 is 0.74. B) $1000\ln\alpha_{g-m}$ is plotted as a function of network–forming elements ($\text{SiO}_2+\text{Al}_2\text{O}_3$) in wt%. The x–axis is inverted. The regression equation in the lower right is Eq. (5) and R^2 is 0.74. The shaded area is a 1–sigma error range.

Fig. 5. This plot illustrates the carbon isotope fractionation coefficient ($1000\ln\alpha_{g-m}$) between CO_2 gas and carbon dissolved in silicate melts, integrating results from our study with literature data from rhyolite (Blank, 1993), MORB (Mattey, 1991), sodamelilite (Mattey et al., 1990), and nephelinite (Petschnig et al., 2024). The graph depicts a scenario where carbon is present in rhyolite only as CO_2 molecular, while the $\text{CO}_3^{2-}/\text{CO}_2$ ratio increases with depolymerization of the melt. It also highlights the limitation of CO_3^{2-} incorporation into silicate melts, indicating the attainment of the maximum $\text{CO}_3^{2-}/\text{CO}_2$ ratio that silicate melts can have around NBO/T=0.88. The solid line represents Eq. (4), while the dashed line extends from the point of Petschnig et al. (2024).

Fig. 6. Isotopic fractionation versus $10^6/T^2$ in K^{-2} for this study and literature data. The solid black line represents the carbonate– CO_2 gas fractionation line derived by Petschnig et al. (2024). The

shaded area is an error estimated by Petschnig et al. (2024). One point from Petschnig et al. (2024) is the nephelinite–CO₂ gas fractionation at 1175 °C and 0.3 GPa.

Fig. 7. A simulation result from rhyolite–MELTS (v.1.2.0) that shows the evolution of isotopic compositions ($\delta^{13}\text{C}$) for gas and melt phases under isobaric conditions at 600 MPa. The starting composition is from melt inclusions from Etna volcano (Gennaro et al., 2019) and the temperature is 1180 °C. The fractionation coefficient changes from 2.9 ‰ to 1.1 ‰ as the melt composition changes. The $\delta^{13}\text{C}_i$ -value is set to be -4 ‰. The dashed line represents the gas $\delta^{13}\text{C}$ -value and the solid line represents the melt $\delta^{13}\text{C}$ -value. BED and FED refer to Batch and Fractional Equilibrium Degassing, respectively. The temperature and corresponding melt fraction remaining in the system are plotted on the bottom and top axes, respectively.

Fig. 8. Semi-quantitative assessment of magmatic processes that can affect the $\delta^{13}\text{C}$ of the melt ($\delta^{13}\text{C}_m$). The fractionation coefficient used here is 2.5 ‰. In a closed system, Batch Equilibrium Degassing (BED) occurs (blue). Fractional Equilibrium Degassing (FED) (orange) results in a significant decrease in $\delta^{13}\text{C}$ -value. Kinetic fractionation (green) may occur during degassing, potentially increasing $\delta^{13}\text{C}$. The dashed green line is the kinetic degassing line for CO₃²⁻ and the solid green line is for CO₂ molecular. The precipitation of carbonatite (red) from the melt has minimal impact on $\delta^{13}\text{C}$. The $\delta^{13}\text{C}_m$ is affected by mixing with carbonate or organic sediment. Mixing with carbonate or organic sediment is assumed to be isobaric.

Declaration of generative AI and AI-assisted technologies in the writing process

During the preparation of this work the authors used DeepL in order to correct grammatical error and improve readability. After using this tool/service, the authors reviewed and edited the content as needed and takes full responsibility for the content of the publication.

References

- Andersen T. and Neumann E.-R. (2001) Fluid inclusions in mantle xenoliths. *Lithos* **55**, 301–320.
- Appora G. (1998) Etude expérimentale du fractionnement isotopique du carbone et de l'oxygène dans les systèmes CO₂-carbonates liquides : application au contexte carbonatitique. Paris Diderot University - Paris 7.
- Aubaud C. (2022) Carbon stable isotope constraints on CO₂ degassing models of ridge, hotspot and arc magmas. *Chemical Geology* **605**, 120962.
- Aubaud C., Pineau F., Jambon A. and Javoy M. (2004) Kinetic disequilibrium of C, He, Ar and carbon isotopes during degassing of mid-ocean ridge basalts. *Earth and Planetary Science Letters* **222**, 391–406.

- Barry P. H., Hilton D. R., Füre E., Halldórsson S. A. and Grönvold K. (2014) Carbon isotope and abundance systematics of Icelandic geothermal gases, fluids and subglacial basalts with implications for mantle plume-related CO₂ fluxes. *Geochimica et Cosmochimica Acta* **134**, 74–99.
- Blank J. G. (1993) An experimental investigation of the behavior of carbon dioxide in rhyolitic melt. California Institute of Technology.
- Blank J. G. and Brooker R. A. (1994) Chapter 5. Experimental studies of carbon dioxide in silicate melts: solubility, speciation, and stable carbon isotope behavior. In *Volatiles in Magmas* (eds. M. R. Carroll and J. R. Holloway). De Gruyter. pp. 157–186.
- Bottinga Y. (1969) Calculated fractionation factors for carbon and hydrogen isotope exchange in the system calcite-carbon dioxide-graphite-methane-hydrogen-water vapor. *Geochimica et Cosmochimica Acta* **33**, 49–64.
- Bourgue E. and Richet P. (2001) The effects of dissolved CO₂ on the density and viscosity of silicate melts: a preliminary study. *Earth and Planetary Science Letters* **193**, 57–68.
- Brandon A. D., Graham D. W., Waight T. and Gautason B. (2007) ¹⁸⁶O_s and ¹⁸⁷O_s enrichments and high-³He/⁴He sources in the Earth's mantle: Evidence from Icelandic picrites. *Geochimica et Cosmochimica Acta* **71**, 4570–4591.
- Brey G. (1976) CO₂ solubility and solubility mechanisms in silicate melts at high pressures. *Contr. Mineral. and Petrol.* **57**, 215–221.
- Brey G. P. and Green D. H. (1976) Solubility of CO₂ in olivine melilitite at high pressures and role of CO₂ in the earth's upper mantle. *Contr. Mineral. and Petrol.* **55**, 217–230.
- Brooker R. A., Kohn S. C., Holloway J. R. and McMillan P. F. (2001) Structural controls on the solubility of CO₂ in silicate melts. *Chemical Geology* **174**, 225–239.
- Cartigny P., Harris J. W., Phillips D., Girard M. and Javoy M. (1998) Subduction-related diamonds? — The evidence for a mantle-derived origin from coupled δ¹³C–δ¹⁵N determinations. *Chemical Geology* **147**, 147–159.
- Cartigny P., Jendzejewski N., Pineau F., Petit E. and Javoy M. (2001) Volatile (C, N, Ar) variability in MORB and the respective roles of mantle source heterogeneity and degassing: the case of the Southwest Indian Ridge. *Earth and Planetary Science Letters* **194**, 241–257.
- Cartigny P., Pineau F., Aubaud C. and Javoy M. (2008) Towards a consistent mantle carbon flux estimate: Insights from volatile systematics (H₂O/Ce, δD, CO₂/Nb) in the North Atlantic mantle (14° N and 34° N). *Earth and Planetary Science Letters* **265**, 672–685.
- Chacko T., Mayeda T. K., Clayton R. N. and Goldsmith J. R. (1991) Oxygen and carbon isotope fractionations between CO₂ and calcite. *Geochimica et Cosmochimica Acta* **55**, 2867–2882.

- Dasgupta R. and Hirschmann M. M. (2010) The deep carbon cycle and melting in Earth's interior. *Earth and Planetary Science Letters* **298**, 1–13.
- Deines P. (2004) Carbon isotope effects in carbonate systems. *Geochimica et Cosmochimica Acta* **68**, 2659–2679.
- Dixon J. E. (1997) Degassing of alkalic basalts. *American Mineralogist* **82**, 368–378.
- Dixon J. E., Edward M. Stolper, and John R. Holloway (1995) An Experimental Study of Water and Carbon Dioxide Solubilities in Mid-Ocean Ridge Basaltic Liquids. Part I: Calibration and Solubility Models. *Journal of Petrology* **36**, 1607–1631.
- Dixon J. E. and Pan V. (1995) Determination of the molar absorptivity of dissolved carbonate in basaltic glass. *American Mineralogist* **80**, 1339–1342.
- Duncan M. S. and Dasgupta R. (2014) CO₂ solubility and speciation in rhyolitic sediment partial melts at 1.5–3.0GPa – Implications for carbon flux in subduction zones. *Geochimica et Cosmochimica Acta* **124**, 328–347.
- Duncan M. S. and Dasgupta R. (2015) Pressure and temperature dependence of CO₂ solubility in hydrous rhyolitic melt: implications for carbon transfer to mantle source of volcanic arcs via partial melt of subducting crustal lithologies. *Contrib Mineral Petrol* **169**, 54.
- Eguchi J. and Dasgupta R. (2018) A CO₂ solubility model for silicate melts from fluid saturation to graphite or diamond saturation. *Chemical Geology* **487**, 23–38.
- Fine G. and Stolper E. (1986) Dissolved carbon dioxide in basaltic glasses: concentrations and speciation. *Earth and Planetary Science Letters* **76**, 263–278.
- Fine G. and Stolper E. (1985) The speciation of carbon dioxide in sodium aluminosilicate glasses. *Contr. Mineral. and Petrol.* **91**, 105–121.
- Fogel R. A. and Rutherford M. J. (1990) The solubility of carbon dioxide in rhyolitic melts; a quantitative FTIR study. *American Mineralogist* **75**, 1311–1326.
- Gaillard F., Malki M., Iacono-Marziano G., Pichavant M. and Scaillet B. (2008) Carbonatite Melts and Electrical Conductivity in the Asthenosphere. *Science* **322**, 1363–1365.
- Gaillard F., Pichavant M. and Scaillet B. (2003) Experimental determination of activities of FeO and Fe₂O₃ components in hydrous silicic melts under oxidizing conditions. *Geochimica et Cosmochimica Acta* **67**, 4389–4409.
- Gennaro E., Iacono-Marziano G., Paonita A., Rotolo S. G., Martel C., Rizzo A. L., Pichavant M. and Liotta M. (2019) Melt inclusions track melt evolution and degassing of Etnean magmas in the last 15 ka. *Lithos* **324–325**, 716–732.
- Goss A. R., Perfit M. R., Ridley W. I., Rubin K. H., Kamenov G. D., Soule S. A., Fundis A. and Fornari D. J. (2010) Geochemistry of lavas from the 2005–2006 eruption at the East

- Pacific Rise, 9°46'N–9°56'N: Implications for ridge crest plumbing and decadal changes in magma chamber compositions. *Geochem Geophys Geosyst* **11**, 2009GC002977.
- Graham D. W., Michael P. J. and Rubin K. H. (2018) An investigation of mid-ocean ridge degassing using He, CO₂, and δ¹³C variations during the 2005–06 eruption at 9°50'N on the East Pacific Rise. *Earth and Planetary Science Letters* **504**, 84–93.
- Grootes P. M., Mook W. G. and Vogel J. C. (1969) Isotopic fractionation between gaseous and condensed carbon dioxide. *Z. Physik* **221**, 257–273.
- Guillot B. and Sator N. (2011) Carbon dioxide in silicate melts: A molecular dynamics simulation study. *Geochimica et Cosmochimica Acta* **75**, 1829–1857.
- Halldórsson S. A., Hilton D. R., Barry P. H., Füre E. and Grönvold K. (2016) Recycling of crustal material by the Iceland mantle plume: New evidence from nitrogen elemental and isotope systematics of subglacial basalts. *Geochimica et Cosmochimica Acta* **176**, 206–226.
- Iacono-Marziano G., Morizet Y., Le Trong E. and Gaillard F. (2012) New experimental data and semi-empirical parameterization of H₂O–CO₂ solubility in mafic melts. *Geochimica et Cosmochimica Acta* **97**, 1–23.
- Ida Di Carlo, Michel Pichavant, Silvio G. Rotolo, and Bruno Scaillet (2006) Experimental Crystallization of a High-K Arc Basalt: the Golden Pumice, Stromboli Volcano (Italy). *Journal of Petrology* **47**, 1317–1343.
- Ionov D. A., Dupuy C., O'Reilly S. Y., Kopylova M. G. and Genshaft Y. S. (1993) Carbonated peridotite xenoliths from Spitsbergen: implications for trace element signature of mantle carbonate metasomatism. *Earth and Planetary Science Letters* **119**, 283–297.
- Jaques A. L., O'Neill H. St. C., Smith C. B., Moon J. and Chappell B. W. (1990) Diamondiferous peridotite xenoliths from the Argyle (AK1) lamproite pipe, Western Australia. *Contr. Mineral. and Petrol.* **104**, 255–276.
- Javoy M. and Pineau F. (1991) The volatiles record of a “popping” rock from the Mid-Atlantic Ridge at 14°N: chemical and isotopic composition of gas trapped in the vesicles. *Earth and Planetary Science Letters* **107**, 598–611.
- Javoy M., Pineau F. and Iiyama I. (1978) Experimental determination of the isotopic fractionation between gaseous CO₂ and carbon dissolved in tholeiitic magma: A preliminary study. *Contr. Mineral. and Petrol.* **67**, 35–39.
- Jendzejewski N., Trull T. W., Pineau F. and Javoy M. (1997) Carbon solubility in Mid-Ocean Ridge basaltic melt at low pressures (250–1950 bar). *Chemical Geology* **138**, 81–92.
- Kamenetsky V. S., Pompilio M., Métrich N., Sobolev A. V., Kuzmin D. V. and Thomas R. (2007) Arrival of extremely volatile-rich high-Mg magmas changes explosivity of Mount Etna. *Geol* **35**, 255.

- Katsura T. (2022) A Revised Adiabatic Temperature Profile for the Mantle. *JGR Solid Earth* **127**, e2021JB023562.
- Kent A. J. R., Peate D. W., Newman S., Stolper E. M. and Pearce J. A. (2002) Chlorine in submarine glasses from the Lau Basin: seawater contamination and constraints on the composition of slab-derived fluids. *Earth and Planetary Science Letters* **202**, 361–377.
- King P. L. and Holloway J. R. (2002) CO₂ solubility and speciation in intermediate (andesitic) melts: the role of H₂O and composition. *Geochimica et Cosmochimica Acta* **66**, 1627–1640.
- Kohn S. C., Brooker R. A. and Dupree R. (1991) ¹³C MAS NMR: A method for studying CO₂ speciation in glasses. *Geochimica et Cosmochimica Acta* **55**, 3879–3884.
- Konschak A. and Keppler H. (2014) The speciation of carbon dioxide in silicate melts. *Contrib Mineral Petrol* **167**, 998.
- Kress V. C. and Carmichael I. S. E. (1991) The compressibility of silicate liquids containing Fe₂O₃ and the effect of composition, temperature, oxygen fugacity and pressure on their redox states. *Contr. Mineral. and Petrol.* **108**, 82–92.
- Le Voyer M., Kelley K. A., Cottrell E. and Hauri E. H. (2017) Heterogeneity in mantle carbon content from CO₂-undersaturated basalts. *Nature Communications* **8**, 14062.
- Lee H. J., Moussallam Y., Rose-Koga E., Piani L., Villeneuve J., Bouden N., Gurenko A., Monteleone B. and Gaetani G. (2024) High-precision determination of carbon stable isotope in silicate glasses by secondary ion mass spectrometry: Evaluation of international standards.
- Leshner C. E. and Spera F. J. (2015) Thermodynamic and Transport Properties of Silicate Melts and Magma. In *The Encyclopedia of Volcanoes* Elsevier. pp. 113–141.
- Macpherson C. G., Hilton D. R., Mertz D. F. and Dunai T. J. (2005) Sources, degassing, and contamination of CO₂, H₂O, He, Ne, and Ar in basaltic glasses from Kolbeinsey Ridge, North Atlantic. *Geochimica et Cosmochimica Acta* **69**, 5729–5746.
- Macpherson C. G., Hilton D. R., Newman S. and Matthey D. P. (1999) CO₂, ¹³C/¹²C and H₂O variability in natural basaltic glasses: a study comparing stepped heating and FTIR spectroscopic techniques. *Geochimica et Cosmochimica Acta* **63**, 1805–1813.
- Macpherson C. and Matthey D. (1994) Carbon isotope variations of CO₂ in Central Lau Basin basalts and ferrobasalts. *Earth and Planetary Science Letters* **121**, 263–276.
- Marty B. and Humbert F. (1997) Nitrogen and argon isotopes in oceanic basalts. *Earth and Planetary Science Letters* **152**, 101–112.
- Matthey D. P. (1991) Carbon dioxide solubility and carbon isotope fractionation in basaltic melt. *Geochimica et Cosmochimica Acta* **55**, 3467–3473.

- Mattey D. P., Exley R. A. and Pillinger C. T. (1989) Isotopic composition of CO₂ and dissolved carbon species in basalt glass. *Geochimica et Cosmochimica Acta* **53**, 2377–2386.
- Mattey D. P., Taylor W. R., Green D. H. and Pillinger C. T. (1990) Carbon isotopic fractionation between CO₂ vapour, silicate and carbonate melts: an experimental study to 30 kbar. *Contr. Mineral. and Petrol.* **104**, 492–505.
- Michael P. J. and Graham D. W. (2015) The behavior and concentration of CO₂ in the suboceanic mantle: Inferences from undegassed ocean ridge and ocean island basalts. *Lithos* **236–237**, 338–351.
- Miller W. G. R., MacLennan J., Shorttle O., Gaetani G. A., Le Roux V. and Klein F. (2019) Estimating the carbon content of the deep mantle with Icelandic melt inclusions. *Earth and Planetary Science Letters* **523**, 115699.
- Morizet Y., Kohn S. C. and Brooker R. A. (2001) Annealing experiments on CO₂-bearing jadeite glass: an insight into the true temperature dependence of CO₂ speciation in silicate melts. *Mineral. mag.* **65**, 701–707.
- Morizet Y., Vuilleumier R. and Paris M. (2015) A NMR and molecular dynamics study of CO₂-bearing basaltic melts and glasses. *Chemical Geology* **418**, 89–103.
- Moussallam Y., Florian P., Corradini D., Morizet Y., Sator N., Vuilleumier R., Guillot B., Iacono-Marziano G., Schmidt B. C. and Gaillard F. (2016a) The molecular structure of melts along the carbonatite–kimberlite–basalt compositional joint: CO₂ and polymerisation. *Earth and Planetary Science Letters* **434**, 129–140.
- Moussallam Y., Morizet Y. and Gaillard F. (2016b) H₂O–CO₂ solubility in low SiO₂-melts and the unique mode of kimberlite degassing and emplacement. *Earth and Planetary Science Letters* **447**, 151–160.
- Moussallam Y., Morizet Y., Massuyeau M., Laumonier M. and Gaillard F. (2015) CO₂ solubility in kimberlite melts. *Chemical Geology* **418**, 198–205.
- Muth M., Duncan M. S. and Dasgupta R. (2020) The Effect of Variable Na/K on the CO₂ Content of Slab-Derived Rhyolitic Melts. In *Geophysical Monograph Series* (eds. C. E. Manning, J. Lin, and W. L. Mao). Wiley. pp. 195–208.
- Mysen B. O., Eggler D. H., Seitz M. G. and Holloway J. R. (1976) Carbon dioxide in silicate melts and crystals; Part I, Solubility measurements. *American Journal of Science* **276**, 455–479.
- Newman S. and Lowenstern J. B. (2002) VolatileCalc: a silicate melt–H₂O–CO₂ solution model written in Visual Basic for excel. *Computers & Geosciences* **28**, 597–604.
- Nichols A. R. L. and Wysoczanski R. J. (2007) Using micro-FTIR spectroscopy to measure volatile contents in small and unexposed inclusions hosted in olivine crystals. *Chemical Geology* **242**, 371–384.

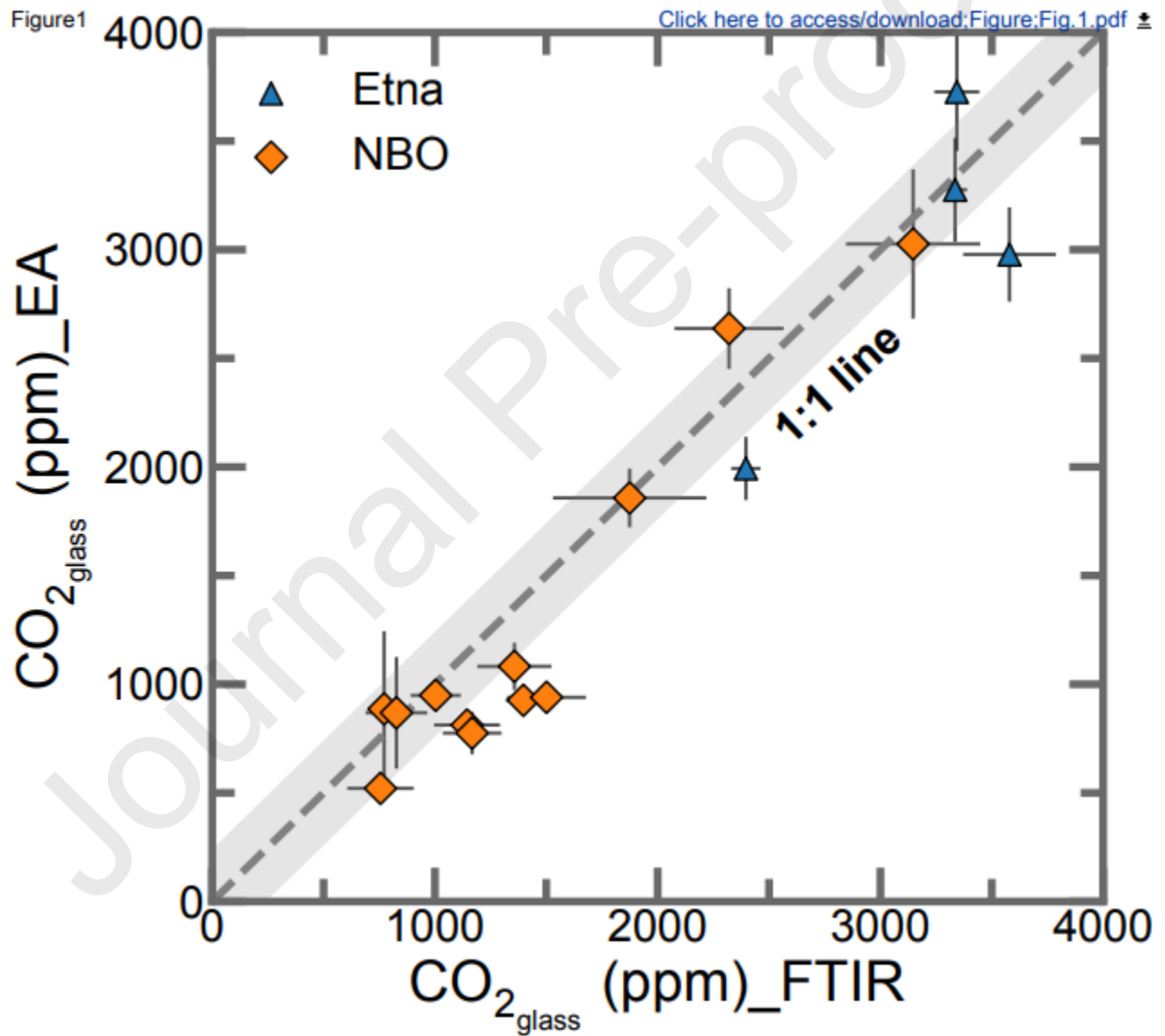
- Nowak M., Porbatzki D., Spickenbom K. and Diedrich O. (2003) Carbon dioxide speciation in silicate melts: a restart. *Earth and Planetary Science Letters* **207**, 131–139.
- Nowak M., Schreen D. and Spickenbom K. (2004) Argon and CO₂ on the race track in silicate melts: A tool for the development of a CO₂ speciation and diffusion model. *Geochimica et Cosmochimica Acta* **68**, 5127–5138.
- O’Neil J. R. (1986) Chapter 1. Theoretical and experimental aspects of isotopic fractionation. In *Stable Isotopes in High Temperature Geological Processes* (eds. J. W. Valley, H. P. Taylor, and J. R. O’Neil). De Gruyter. pp. 1–40.
- Paillat O., Elphick S. C. and Brown W. L. (1992) The solubility of water in NaAlSi₃O₈ melts: a re-examination of Ab-H₂O phase relationships and critical behaviour at high pressures. *Contr. Mineral. and Petrol.* **112**, 490–500.
- Paonita A., Caracausi A., Iacono-Marziano G., Martelli M. and Rizzo A. (2012) Geochemical evidence for mixing between fluids exsolved at different depths in the magmatic system of Mt Etna (Italy). *Geochimica et Cosmochimica Acta* **84**, 380–394.
- Pearce J. A., Ernewein M., Bloomer S. H., Parson L. M., Murton B. J. and Johnson L. E. (1994) Geochemistry of Lau Basin volcanic rocks: influence of ridge segmentation and arc proximity. *SP* **81**, 53–75.
- Pearson D. G., Boyd F. R., Haggerty S. E., Pasteris J. D., Field S. W., Nixon P. H. and Pokhilenko N. P. (1994) The characterisation and origin of graphite in cratonic lithospheric mantle: a petrological carbon isotope and Raman spectroscopic study. *Contr. Mineral. and Petrol.* **115**, 449–466.
- Petschnig P., Schmidt M. W., Kueter N., Sartori G. and Bernasconi S. M. (2024) An almost universal CO₂-CO₃²⁻ carbon isotope fractionation function for high temperatures. *Earth and Planetary Science Letters* **627**, 118552.
- Pineau F. and Javoy M. (1983) Carbon isotopes and concentrations in mid-oceanic ridge basalts. *Earth and Planetary Science Letters* **62**, 239–257.
- Pineau F., Shilobreeva S., Hekinian R., Bideau D. and Javoy M. (2004) Deep-sea explosive activity on the Mid-Atlantic Ridge near 34°50’N: a stable isotope (C, H, O) study. *Chemical Geology* **211**, 159–175.
- Rosenbaum J. M. (1994) Stable isotope fractionation between carbon dioxide and calcite at 900°C. *Geochimica et Cosmochimica Acta* **58**, 3747–3753.
- Saal A., Hauri E., Langmuir C. H. and Perfit M. (2002) Vapour undersaturation in primitive mid-ocean-ridge basalt and the volatile content of Earth’s upper mantle. *Nature* **419**, 451.
- Sano Y. and Marty B. (1995) Origin of carbon in fumarolic gas from island arcs. *Chemical Geology* **119**, 265–274.

- Scheele N. and Hoefs J. (1992) Carbon isotope fractionation between calcite, graphite and CO₂: an experimental study. *Contrib Mineral Petrol* **112**, 35–45.
- Sharp Z. (2017) Principles of Stable Isotope Geochemistry, 2nd Edition.
- Shaw A. M., Hilton D. R., Macpherson C. G. and Sinton J. M. (2004) The CO₂-He-Ar-H₂O systematics of the manus back-arc basin: resolving source composition from degassing and contamination effects. *Geochimica et Cosmochimica Acta* **68**, 1837–1855.
- Shishkina T. A., Botcharnikov R. E., Holtz F., Almeev R. R., Jazwa A. M. and Jakubiak A. A. (2014) Compositional and pressure effects on the solubility of H₂O and CO₂ in mafic melts. *Chemical Geology* **388**, 112–129.
- Sierralta M., Nowak M. and Keppler H. (2002) The influence of bulk composition on the diffusivity of carbon dioxide in Na aluminosilicate melts. *American Mineralogist* **87**, 1710–1716.
- Solomatova N., Caracas R. and Cohen R. (2020) Carbon Speciation and Solubility in Silicate Melts. In *Geophysical Monograph Series* (eds. C. E. Manning, J. Lin, and W. L. Mao). Wiley. pp. 179–194.
- Spickenbom K., Sierralta M. and Nowak M. (2010) Carbon dioxide and argon diffusion in silicate melts: Insights into the CO₂ speciation in magmas. *Geochimica et Cosmochimica Acta* **74**, 6541–6564.
- Stolper E. (1982) The speciation of water in silicate melts. *Geochimica et Cosmochimica Acta* **46**, 2609–2620.
- Stolper E. and Holloway J. R. (1988) Experimental determination of the solubility of carbon dioxide in molten basalt at low pressure. *Earth and Planetary Science Letters* **87**, 397–408.
- Sun C. and Dasgupta R. (2023) Carbon budget of Earth's deep mantle constrained by petrogenesis of silica-poor ocean island basalts. *Earth and Planetary Science Letters* **611**, 118135.
- Taylor B. E. (1986) Chapter 7. Magmatic volatiles: Isotopic variation of C, H, and S. In *Stable Isotopes in High Temperature Geological Processes* (eds. J. W. Valley, H. P. Taylor, and J. R. O'Neil). De Gruyter. pp. 185–226.
- Trull T. W., Pineau F., Bottinga Y. and Javoy M. (1992) CO₂ bubble growth and ¹³C/¹²C isotopic fractionation in basaltic melt. *Eos (Washington, D.C.)* **73**, 348.
- Wardell L. J., Kyle P. R. and Chaffin C. (2004) Carbon dioxide and carbon monoxide emission rates from an alkaline intra-plate volcano: Mt. Erebus, Antarctica. *Journal of Volcanology and Geothermal Research* **131**, 109–121.

Webster J. D. and De Vivo B. (2002) Experimental and modeled solubilities of chlorine in aluminosilicate melts, consequences of magma evolution, and implications for exsolution of hydrous chloride melt at Mt. Somma-Vesuvius. *American Mineralogist* **87**, 1046–1061.

Yoshino T., McIsaac E., Laumonier M. and Katsura T. (2012) Electrical conductivity of partial molten carbonate peridotite. *Physics of the Earth and Planetary Interiors* **194–195**, 1–9.

Zhang Y., Xu Z., Zhu M. and Wang H. (2007) Silicate melt properties and volcanic eruptions. *Reviews of Geophysics* **45**, 2006RG000216.



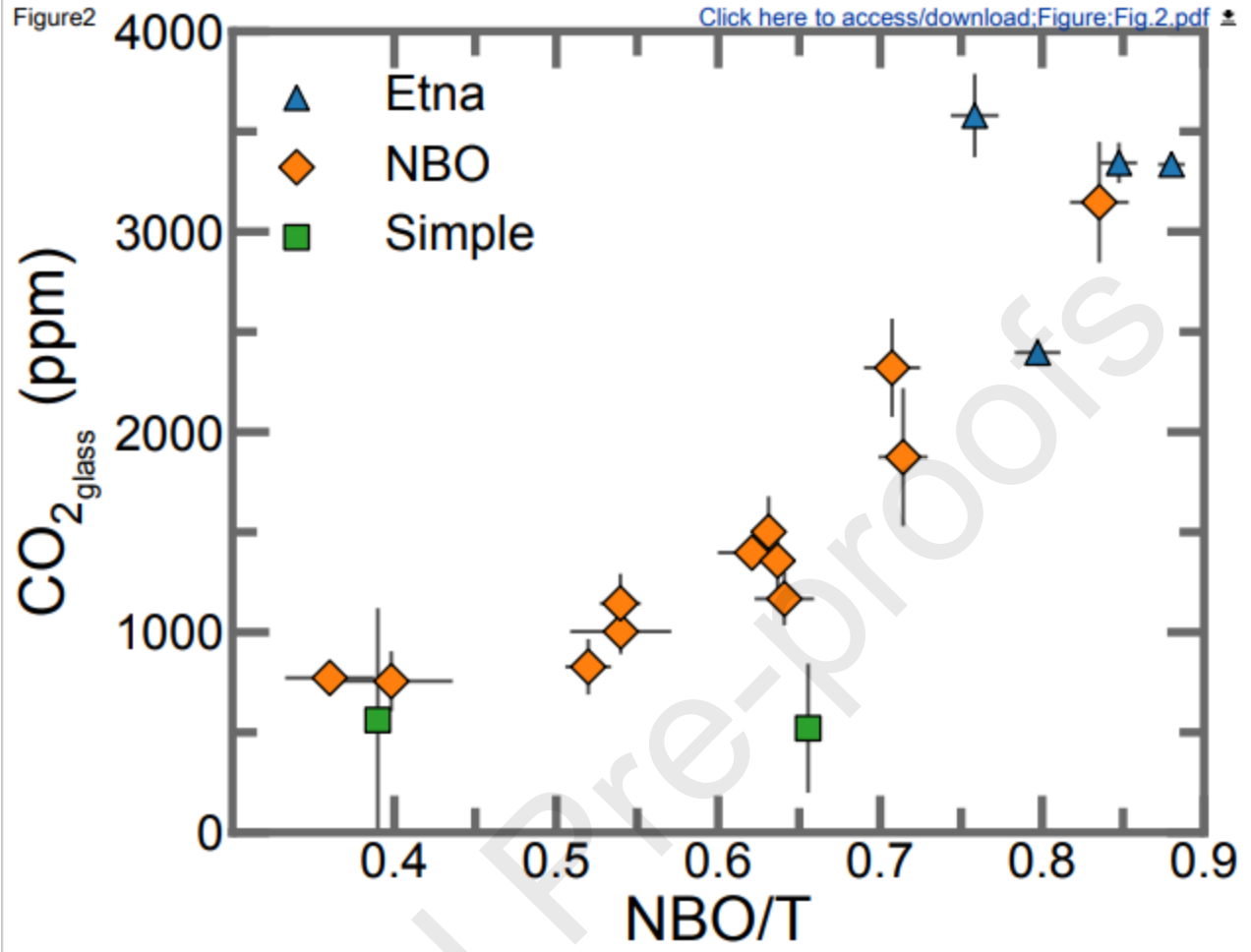


Figure3

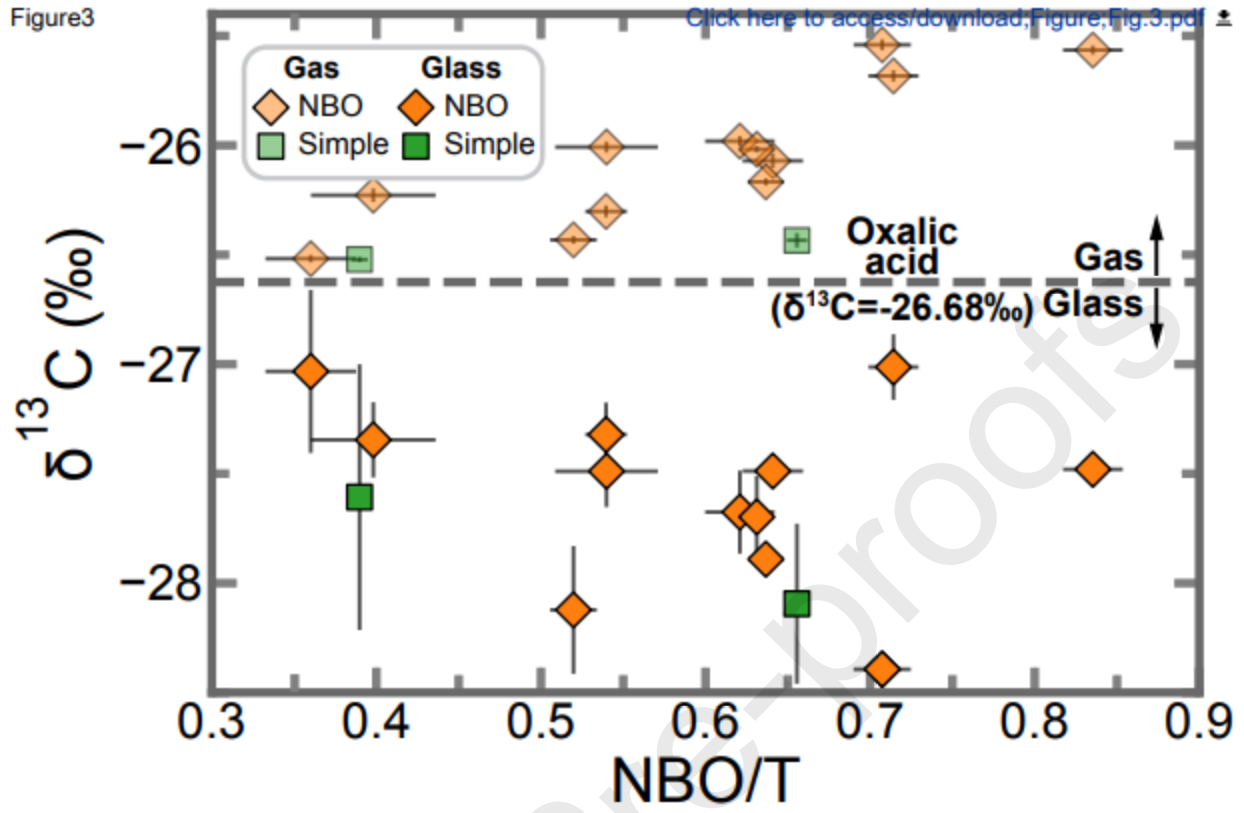


Figure4

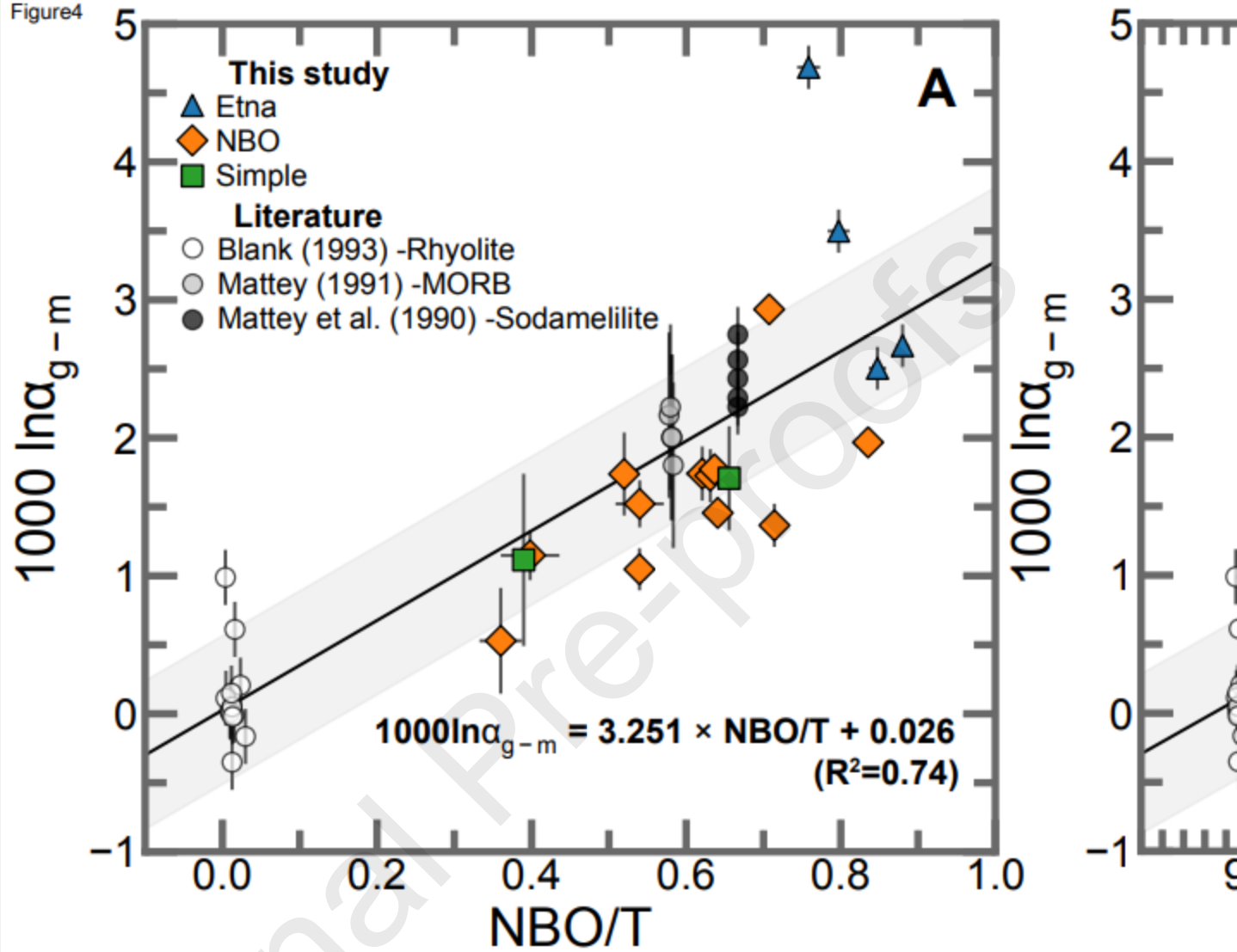


Figure5

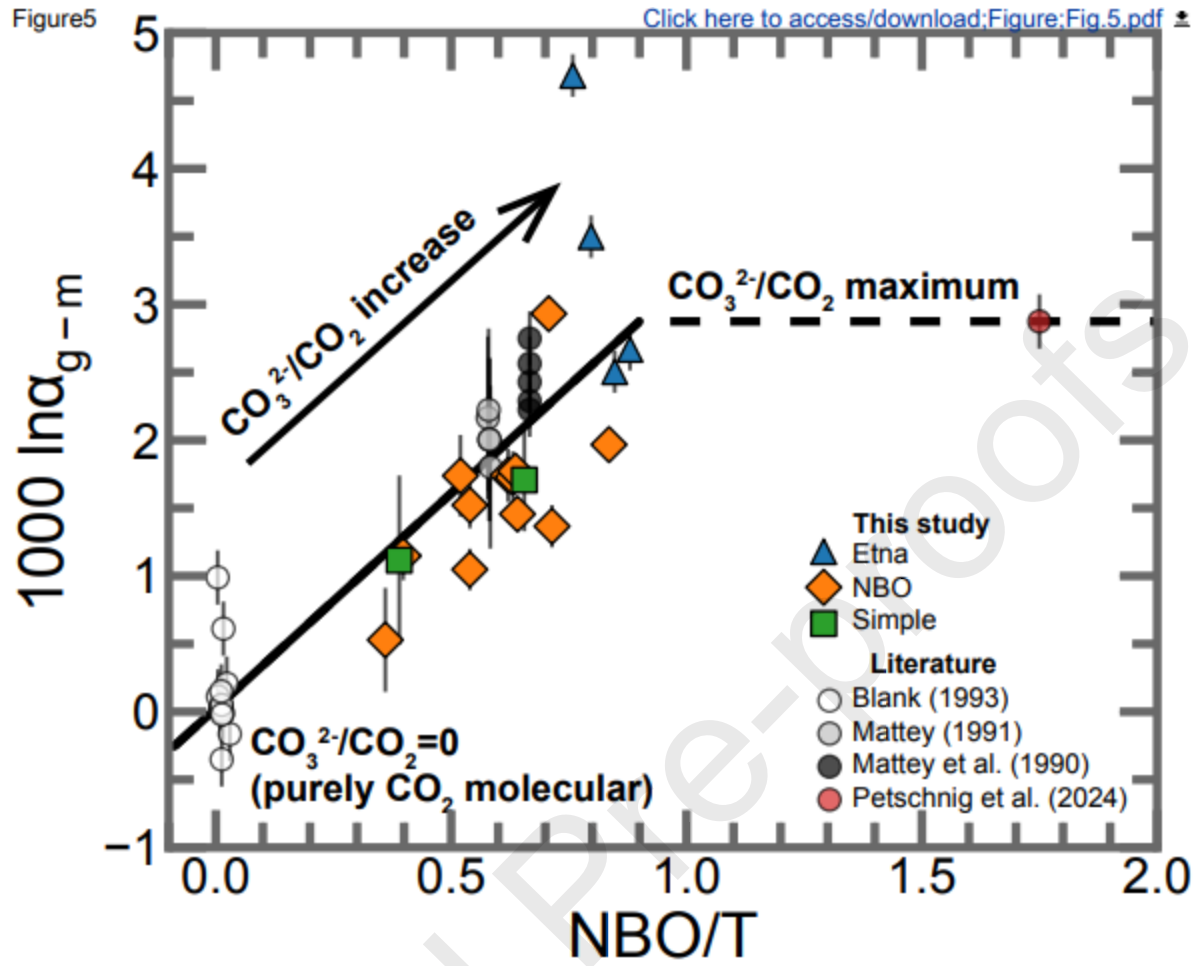


Figure 6

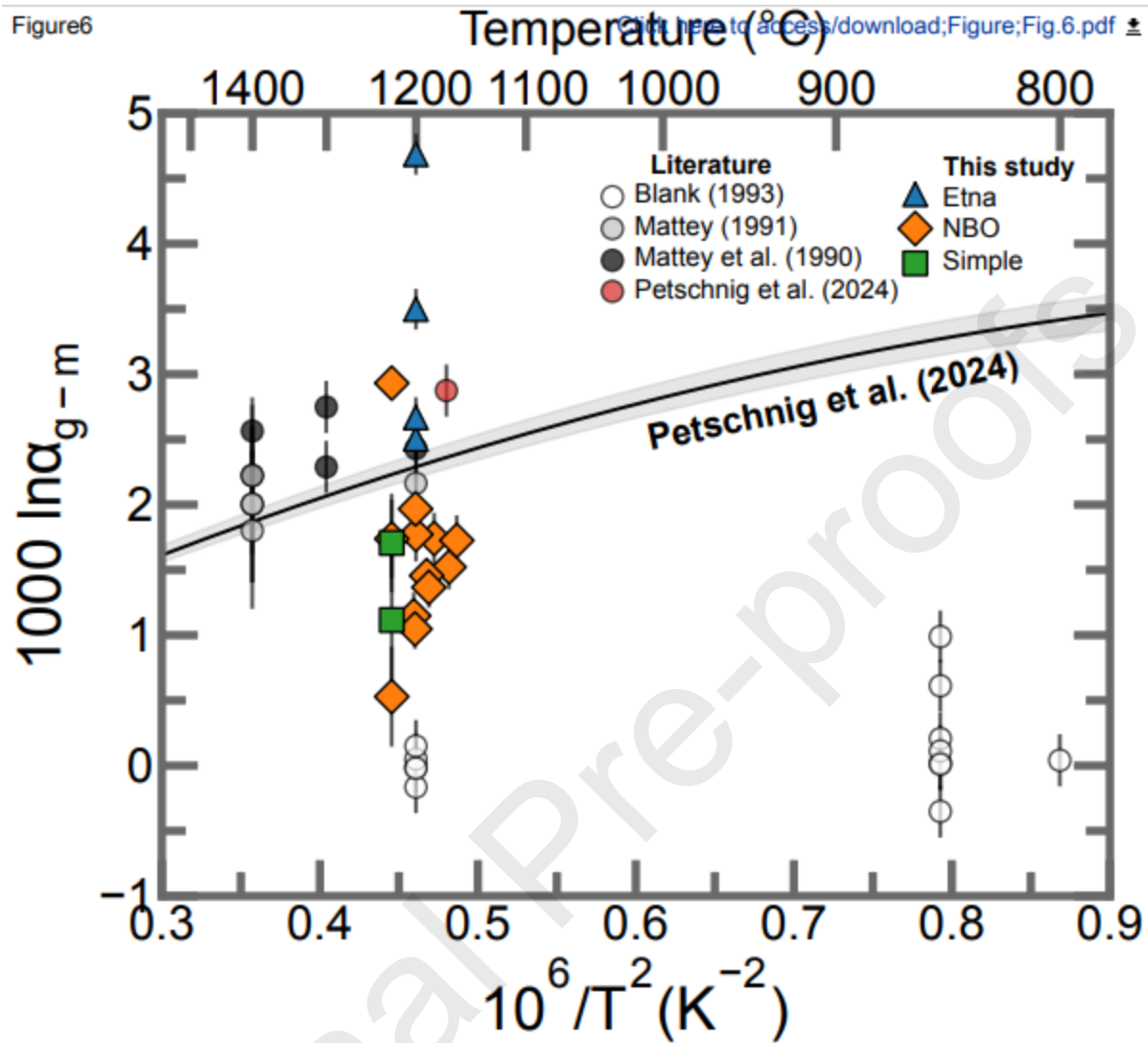


Figure 7

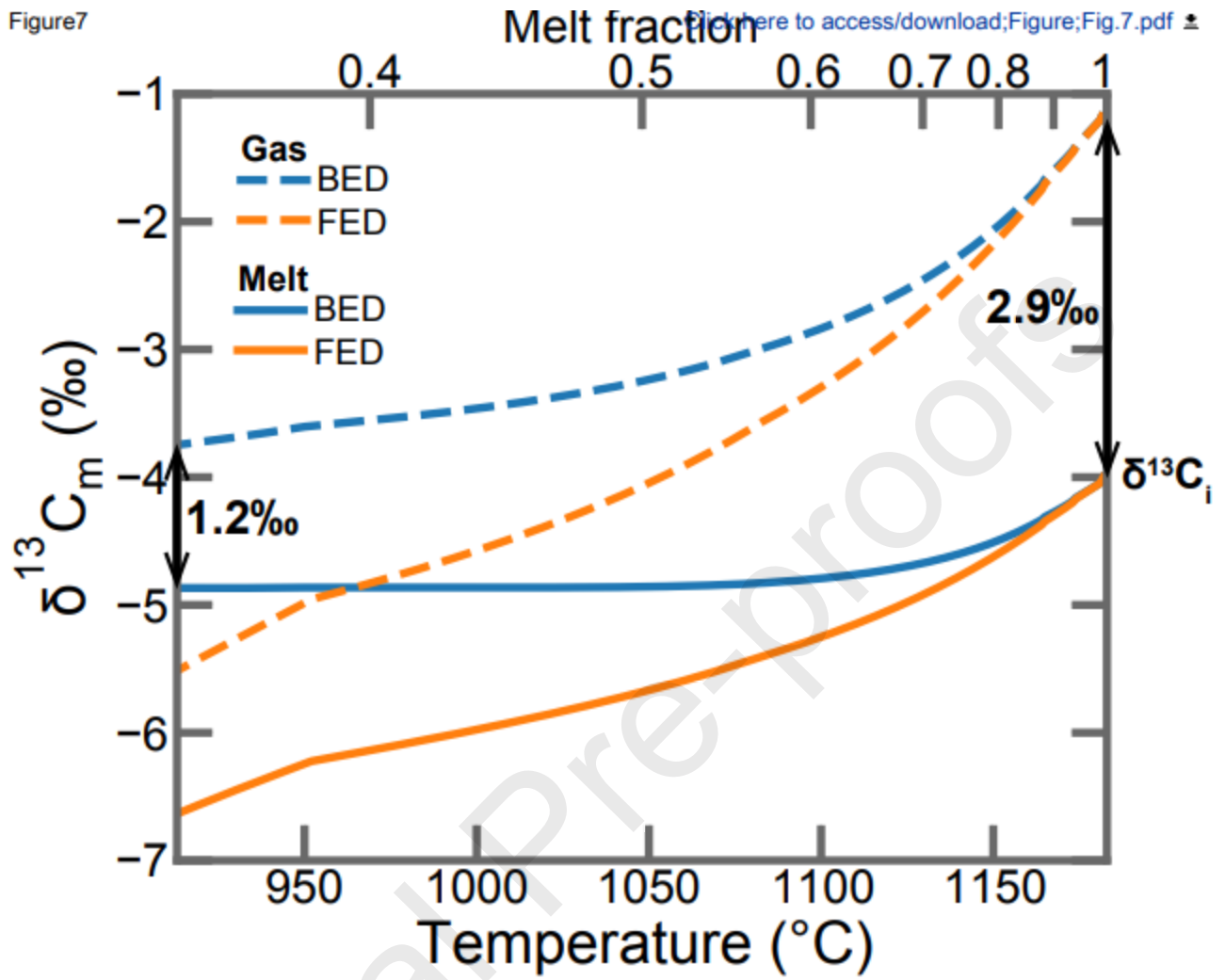


Figure 8

[Click here to access/download;Figure;Fig.8.pdf](#)